Title

WWOX deficiency impairs neurogenesis and neuronal function in human organoids

Authors

Daniel J. Steinberg[1,†], Asia Zonca[2,†], Idan Rosh[3], Irina Kustanovich[3], Kian Maroun[1], Shani Stern[3], Jose Davila-Velderrain[2,*], Rami I. Aqeilan[1,*]

Affiliations

[1]The Concern Foundation Laboratories, The Lautenberg Center for Immunology and Cancer Research, Department of Immunology and Cancer Research-IMRIC, Hebrew University of Jerusalem, Jerusalem, Israel;

[2]Human Technopole, Viale Rita Levi-Montalcini 1, 20157, Milan, Italy.

[3]Sagol Department of Neurobiology, University of Haifa, Israel

† These authors contributed equally to this work

* Corresponding authors and lead contacts: ramiaq@mail.huji.ac.il, jose.davila@fht.org

Abstract

WOREE and SCAR12 syndromes are rare neurodevelopmental disorders caused by WWOX mutations, severely impairing brain development. The pleiotropic nature of WWOX complicates identifying specific mechanisms. Using neural organoids and single-cell transcriptomics, we identified radial glial cells (RGs) as preferentially affected, with disrupted cell cycle dynamics leading to an accumulation of cells in the G2/M and S phases, overexpression of the proto-oncogene MYC, and concomitant reduction in neuronal generation. Patient-derived organoids exhibited milder phenotypes compared to knockout organoids, showing functional neuronal impairments like hyperexcitability and delayed differentiation rather than RG dysfunction. Remarkably, gene therapy restored neuronal function, normalizing hyperexcitability and promoting maturation, without disturbing RG populations. We propose a model in which WWOX mutations impair neurogenesis via RG through cell-type specific dysregulation of the MYC and Wnt signaling pathways. These insights highlight potential therapeutic strategies for WWOX-related disorders and open avenues for interventions targeting these key molecular pathways.

Teaser

WWOX mutations disrupt radial glial function and neurogenesis via MYC dysregulation, with gene therapy offering targeted restoration.

MAIN TEXT

Introduction

WWOX-related epileptic encephalopathy (WOREE syndrome) and Spinocerebellar ataxia autosomal recessive type 12 (SCAR12 syndrome) are rare and devastating neurodevelopmental disorders linked to mutations in the WW-domain containing oxidoreductase *(WWOX)* gene (*1–3*). The typical symptoms for both disorders include early-onset epilepsy, cognitive impairments, global developmental delay, structural brain abnormalities and atrophy, and in some cases, premature death (*4, 5*). These WWOX-related neurodevelopmental disorders display gradual severity in genotype-phenotype associations (*4*). First, SCAR12 syndrome has been diagnosed so far only in patients with missense mutations (*2*), while WOREE is commonly associated with nonsense mutations and copy number variations (*5*). Second, both survival and time-to-seizure onset analyses for 75 individuals with WOREE syndrome showed worst prognosis in individuals with null-mutations, whose severity correlated with the number of null-alleles (*6*).

The *WWOX* gene, mostly studied for its tumor suppressor effect, is known to influence a wide array of biological processes, often by functioning as an adaptor protein and transcriptional co-repressor (*7*), making its cellular effects context-dependent, varying according to the available binding partners. *WWOX* expression levels also vary during development. In human brain tissue samples WWOX transcription levels are relatively high in early embryonic life and progressively decrease during fetal development until birth, after which expression increases gradually and remains high from adolescence onwards (*8*). *In-vitro* study of brain development further demonstrated a similar pattern of differential *WWOX* expression during development and highlighted its connection to epilepsy (*9*). However, whether similar developmental patterns of WWOX expression are recapitulated in experimental models of human neurodevelopment and how they relate to changes in cellular composition remains unclear.

Human neurogenesis is a highly dynamic process, involving diverse transitions between cellular populations. During embryonic development, neural induction gives rise to columnar neuroepithelial cells (NE), often referred to as the neuroectoderm (*10*). These cells line the ventricle creating a germinal zone, referred to as the ventricular zone (VZ). Around gestational week 7 (GW7), the NE cells acquire astroglia characteristics and transition into radial glia (RG) cells (*11–13*). Around GW11 (*14, 15*) certain RG cells transform, disconnecting their apical processes, becoming unipolar, and migrating away from the VZ (*16–18*). Accordingly, RGs subdivide into those that line the ventricle (ventricular RGs or vRGs, also known as apical RGs or aRGs), and those that migrate (outer or oRGs, also basal RGs or bRGs) (*11, 19*). In this transformation oRGs inherit the basal process, which eventually leads to the entirety of vRGs disconnecting from the meninges and becoming truncated RG (tRG) cells midway into neurogenesis (around GW16.5) (*17, 20*). All neural stem cell (NSC) subtypes and their progenies are thus derived from the VZ. WWOX was shown to be most expressed in the VZ in neural organoids (*21*). This pattern, together with the neurodevelopmental implications of WWOX loss on patients, highlights the importance of WWOX in proper CNS

development and neurogenesis. However, the specific molecular pathways affected by *WWOX* deficiency and how they contribute to disease pathogenesis is poorly understood.

In recent years, neural organoids have emerged as a revolutionary tool to model human brain development and disease in vitro (*22*). Neural organoids have been particularly useful in experimentally dissecting cellular heterogeneity in neurogenesis (*23*).

Our previous studies of WWOX deficient organoids indeed revealed that multiple disease-relevant phenotypes like hyperexcitability and cellular composition abnormalities can be recovered and rescued by restoration of WWOX expression *in-vitro* (*21*). Macroscopic examination to these organoids with immunostaining and bulk RNA sequencing also suggested apparent changes in cellular populations and hypomyelination (*21, 24*). However, what specific cell types and neurodevelopmental processes were affected the most by WWOX deficiency and how to ameliorate these alterations with clinically relevant therapeutic strategies remains an open challenge. To address these problems, in the present study we investigate the molecular, cellular, and functional consequences of WWOX mutations at cellular resolution by combining neural organoids derived from *WWOX*-deficient iPSCs and patient cells with single-cell transcriptomic profiling, reanalysis of human fetal data, and electrophysiological recordings. We discovered preferential expression of WWOX in RG cells, where its deficiency leads to impaired cell cycle progression, increased MYC expression, and reduction of neuronal generation, processed potentially mediated by Wnt pathway activation. Patient-derived organoids showed a less severe phenotype than that seen in KO organoids, with generation of functionally impaired neurons that can be rescued with gene therapy.

Results

Generation of WWOX-deficient neural organoids

While WWOX mutations cause severe neurodevelopmental disorders, the molecular mechanisms underlying its role in human brain development remain poorly understood. To experimentally dissect the role of WWOX deficiency in human neurodevelopment, we generated unguided neural organoids, often referred to as cerebral organoids (COs) (*25*), for wildtype (WT), WWOX knocked-out (WWOX-KO), and patient-derived (WOREE or SCAR12) conditions (**Fig. 1A**). We established a WT iPSC line from a healthy adult male donor (JH-iPS11) (**Fig. S1A**). We knocked-out WWOX in this line using the CRISPR/Cas9 system (**Fig. S2A**) to establish KO lines (two selected subclones JH-iPS11 WKO-1C and WKO-2C). We used previously reported WOREE and SCAR12 iPSCs (Steinberg et al., 2021) for patient-derived lines and acquired new fibroblast isolated from skin biopsies of an additional WOREE patient (*6*). This additional individual has a complex heterozygous WWOX mutation: a maternal c.864G>A nonsense mutation and a paternal 0.9 Mb deletion spanning arr[GRCh37]16q23.1(78356662_78450052) speculated to result in the absence of exon 6. We reprogrammed these fibroblasts to iPSCs (**Fig. S1C**) and termed the resulting line LM-iPS (**Fig. 1A**). We confirmed the presence of the mutations in affected individuals through gel electrophoresis (**Fig. S1E**) and Sanger sequencing (**Fig. S1F**) of cDNA samples. WWOX-expression assessment with

immunoblot (**Fig. S1D**) revealed a decrease in protein level in the affected individual compared to samples derived from the unaffected heterozygote parents.

Using this diverse iPSC cohort of WT, WWOX-KO, WOREE, and SCAR12 iPSCs (**Fig. 1A**) we established unguided organoids and assessed with immunofluorescence the presence of ventricular zone (VZ) and cortical plate (CP) structure at week 7 (**Fig. 1B**). This analysis confirmed high WWOX expression in the VZ and reduced expression in all mutant lines. Cell-attached electrophysiological recordings of the organoids confirmed increased neuronal activity in WWOX-deficient organoids, consistent with the ability of *in-vitro* systems to recapitulate disease-relevant phenotypes (*21, 24*) (**Fig. 1C and Fig. S1G**; **Fig. 1D**). Notably, SCAR12 patient-derived organoid recordings also showed hyperexcitability, a novel finding consistent with the epileptic seizures seen in patients (*2*) and with findings from a rodent model (*26*).

Given the prominent expression of WWOX in the VZ, a critical neurogenic niche that orchestrates cortical architecture and cellular composition, we investigated alterations in early neurogenesis by analyzing the balance between RGs and nascent neurons during initial organoid development. We focused our analysis on week 7 organoids, which primarily contain NSCs and early-born preplate neurons (*27*). To assess this balance at tissue resolution, we employed two marker genes: SOX2, a transcription factor expressed in neural progenitors, and SATB2, a major determinant expressed early in upper layer neuron specification and expressed in a wide variety of developing neurons (*28–32*). Immunofluorescence analysis revealed a significant reduction in SATB2-positive cells concurrent with an expansion of the SOX2-positive population in WWOX-mutant organoids compared to controls (**Fig. 1E** and **Fig. 1F**). This reciprocal relationship between SOX2 and SATB2 expression suggests impaired transition from RGs to neurons. The severity of this neurogenic disruption demonstrated a genotype-dependent gradient, with WWOX knockout organoids exhibiting the most pronounced phenotype, followed by WOREE and SCAR12 variants, thus correlating with the overall phenotypic severity of human patients.

Impaired neurogenesis in WWOX-mutated organoids through scRNA-seq

To examine the cellular and molecular composition of our organoids, we performed single-cell RNA sequencing (scRNA-seq) on organoids dissociated at week 16 using an established protocol (*33*) (**Fig. 2A-B**, and **Fig. S2A-B**). To identify the main cellular identities recapitulated by our experimental system, we grouped all cells jointly into 12 transcriptionally similar clusters following dimensional reduction and batch-correction analyses (Methods) (**Supplementary Fig. 2A**). By comparing these groups with cell type profiles from human fetal data (*34–37*) and assessing the expression of known marker genes, we identified all major expected cell types, including RGs, neural progenitor cells (NP) (also referred to as intermediate progenitors), and neurons (Neu) (**Fig. 2A-D** and **Fig. S2B-E**). Based on these comparisons, the total RGs population could be further interpreted in subsets of outer RGs (oRGs), cycling RGs (cRGs), and a mixed population of vRGs, neuroectodermal cells, and glial progenitor cells (RG) (**Fig. 1A** and **Fig. S2C-D**).

Notably, WWOX-KO and WOREE organoids showed a prominent increase in the relative number of total recognized RG cells (RGs) (**Fig. 2D-F**), while SCAR12 organoids (modeling a relatively milder disease) exhibited an RG population similar to WT. This result was more pronounced in the WWOX-KO organoids, compared to the WOREE organoids. Concomitant to this cellular phenotype, WWOX-KO organoids also showed a dramatic decrease in identified neurons relative to WT organoids (**Fig. 2F)**. Importantly, this was not the case in our patient-derived organoids. Although some changes could be observed in the cells interpreted as neural progenitors, oRGs or cRGs, due to the known heterogeneity of unguided organoids, we abstained from drawing conclusions at such finer resolution.

Inverse relationship between MYC and WWOX expression through brain development and in neural organoids

Our current and previous data indicates that WWOX is expressed the highest in the ventricular□like zone (VZ) of human organoids at tissue-resolution (*21*) (**Fig. 1B**). Therefore, the impact of WWOX-deficiency on neurogenesis might primarily result from alterations to the cellular populations constituting this zone. To investigate developmental WWOX expression at higher resolution in this zone *in vitro* and *in vivo*, we complemented our organoids data with previously published transcriptomic data from human fetal samples at tissue-dissected (*38*), cell-sorted (*39*), single-cell (*36*), and temporal resolutions (*40*). This multi-resolution analysis allowed us to further characterize WWOX expression patterns at cellular resolution across different developmental stages. Consistent with our observations in organoids, WWOX was preferentially expressed in RG cells *in vivo* at single-cell level at post-conceptional week 16 (**Fig. 3A-C**) and at bulk-level in $SOX2^{+}PAX6^{+}$ RG cells isolated from the germinal zone (GZ) of human cortical samples using fluorescence-activated cell sorting (FACS) (**Fig. 3D**), suggesting that the source of high WWOX expression in the fetal brain and in the VZ is the RGs and demonstrating that this pattern is not an artifact of the organoid system.

Because the most striking changes in the RGs population in our organoids were observed in the KO genotype, we focused on the comparison between RGs from the WT and WWOX-KO organoids to uncover potential molecular alterations mediating WWOX-deficient phenotypes (**Fig. 3E**). Differential gene expression analysis of WWOX-KO vs WT RG cells identified the proto-oncogene MYC (also known as c-Myc) as the top significantly upregulated gene in WWOX-deficient RGs (**Fig. 3F**). This result is consistent with a previous observation of MYC overexpression upon WWOX ablation in osteosarcoma (*41*). However, this is, to our knowledge, the first time that an inverse relationship between WWOX and MYC has been observed in non-neoplastic tissue. To investigate whether this inverse association is recapitulated *in vivo* and reproducible *in-vitro*, we analyzed MYC and WWOX expression patterns across cortical zones of the fetal human brain at mid-gestation (*38*) (**Fig. 3G**) and across developmental time in human forebrain samples (*40*) (**Fig. 3H**). In both cases a clear inverse correlation emerged in which increasing WWOX expression coincides with decreasing MYC expression and vice versa. This pattern was also reproduced in an independent transcriptomic dataset of human neural organoid maturation (*9*) (**Fig. 3I**).

To validate these transcriptional patterns at protein level, we immunostained our week 16 organoids and found a significant increase in cells double positive for SOX2 and MYC (**Fig. 3J** and **Fig. 3K**). This increase in MYC expression was observed also in the RGs from SCAR12 and WOREE organoids (**Fig. 3J-K** and **Fig. S3A-D**). To further validate this observation in an independent *in vitro* system, we modeled WWOX-deficient NE and RG cells in 2D by differentiating neural stem cells (NSCs) from our previously described WWOX-KO WiBR3 human embryonic stem cell (hESC) system (*21*) using an established protocol (*42*) (**Fig. S4A**). These cells expressed high levels of SOX2 and β3-tubulin, and WWOX in the WT NSCs (**Fig. S4A**), confirming their identity. Immunoblot and immunostaining of these cells confirmed high MYC expression upon WWOX-KO (**Fig. 3L** and **Fig. S4B-C**).

Altogether, our data uncovered a reproducible inverse relationship between WWOX and MYC, extending this association from cancer to neurodevelopment. This relationship seems to be robust across brain development, as it is evident not only in our in vitro models, but also in reference fetal and organoids datasets, and in both WOREE and SCAR12 organoids.

Cell-cycle and potency abnormalities in WWOX-deficient MYC-overexpressing RGs

The MYC gene is a well-known regulator of cell proliferation and differentiation, and its dysregulation has been implicated in cell cycle control disruption in various contexts (*43–46*). To investigate potential cell cycle alterations in WWOX-mutated RGs, we estimated deviations in cell cycle progression between WT and WWOX-KO organoids by inferring cell cycle state from single-cell expression using a previously established computational tool *tricycle* (*47*). Inference is based on estimating per cell a continuous cell-cycle pseudotime that represents progression through the cell-cycle phases (Methods). This analysis revealed an increase in the fraction of RGs with an estimated S (0.5π - 1π pseudotime) or G2M (1π - 0.5π) cell cycle state in WWOX-KO organoids compared to WT, suggesting cell cycle alterations in RG under WWOX deficiency (**Fig. 4A-C**). This is consistent with the known MYC effects on cell cycle, including acceleration of the transit through G1/S and prolongation of the G2/M phases (*46, 48, 49*). Radial glial cells estimated to be in G2/M or S phases also expressed higher levels of MYC compared to G1/G0 and M phase cells in WWOX-KO organoids but not in WT (**Fig. 4D**).

Next, since MYC is known to maintain the potency of PSCs (*50*) and was shown to block the differentiation of neural progenitors to postmitotic neurons in the mouse embryo (*51*), we hypothesized that it might have a similar effect in RG cells following loss of WWOX. To look for transcriptomic evidence of this, we classified RG cells in three groups from low to high commitment level based on "potency scores" estimated from single-cell expression using a previously established machine learning algorithm *CytoTrace2* (*52*). Most WWOX-KO RGs were estimated to have a high potency state, while WT RGs showed a low-potency state (**Fig. 4E-G** and **Fig. S5A**), possibly supporting a notion of MYC-associated impaired differentiation. Pathway enrichment analysis of the cells in different pluripotency states revealed overrepresentation of genes involved in cell cycle, DNA replication, and cellular senescence in high potency cells (**Fig. S5B**). This was further supported by high levels of p53 in WWOX-KO NSCs (**Fig. S5C**). To test for

associations between genotype, potency state, and cell cycle phase we performed statistical overrepresentation analysis. We found that high-potency RGs are overrepresented within WWOX-KO cells and cells in S - G2/M phases, while low-potency RGs are enriched within WT cells and cells in G1/G0 - M phases (**Fig. 4H**). To find additional evidence of MYC-mediated differentiation impairment of RG cells, we compiled from an integrative database target-genes with evidence of positive or negative regulation by MYC (i.e., regulons) and tested their association with RG potency states (Methods). WWOX-KO high-potency cells preferentially express target genes positively regulated by MYC, further suggesting a mediating role of MYC in impaired RG differentiation (**Fig. 4I**). Negatively regulated targets did not show an association. Further supporting this MYC-dependent mechanism, the Wnt pathway, which can induce expression of MYC and vice versa (*53, 54*), was previously been shown to be activated in WWOX-mutated organoids (*21*). In line with these findings, our current enrichment analysis of Wnt signaling genes also showed evidence of association of this pathway with high-potency RGs (**Fig. 4I**). Medium-potency cells showed similar enrichment for MYC regulons and Wnt signaling, while low-potency cells did not show an association.

Early gene expression signature in WOREE- and SCAR12-derived neurons

After having established a role for WWOX-deficiency in neurogenesis through alterations in early progenitors, we next sought to analyze potential consequences of additional alterations in the generated neuronal populations in our organoids. Due to the low number of neurons generated in WWOX-KO organoids (**Fig. 2E**), the analysis focused on WOREE- and SCAR12-derived neurons (**Fig. 5A**). We isolated, combined, and re-clustered the cells transcriptionally identified as NP or neurons in the initial analysis of the scRNA-seq data (**Fig. 2A** and **Fig. S6A**). We included NP cells to consider potential early alterations on identity specification. This resulted in 11 neuronal (ExN) clusters which were then compared to reference developmental neuronal cell types for interpretation (*55*) (**Fig. S6B**). We defined 7 subgroups of neurons (**Fig. 5B** and **Fig. S6C**) with signatures corresponding to deep-layer excitatory neurons, as well as newborn and immature neurons. Based on transcriptional similarity with signatures of neuronal subpopulations sequentially observed in fetal neurogenesis, we further classified these 7 subgroups into two general groups – neurons with a gene signature resembling early or late developmental stages during neurogenesis. Cells interpreted as having an early expression signature correlate with *in-vivo* signatures of NP, immature, and newborn neurons, while those with late signatures primarily correlate with L5 and L6 excitatory neurons. A subset of late neurons (mixed) correlated with signatures of both excitatory and inhibitory neurons (**Fig. S6B**). Early cells express regulators of the initial specification of neocortical cell fate (e.g., PAX6, EMX2, and FOXG1) and the immature marker DCX, and are overrepresented with pathways involved in biosynthesis, neuron differentiation, Wnt signaling, and cell proliferation. In contrast, late cells express regulators of the postmitotic specification of deep-layer neurons (e.g., FEZF2, and BCL11B/CTIP2), the calcium sensor SYT1, voltage-gated sodium and potassium channel subunits (e.g., SCN2A, SCN1A, KCNA3, KCNA4), and are overrepresented with pathways involved in carbohydrate metabolism, neurotransmitter secretion, synapses, and membrane

depolarization (**Fig. 5C** and **Fig. 5D**). Although neurons of both groups appeared in all three organoids analyzed, so-called "early cells" were enriched in the WOREE- and SCAR12-derived organoids (**Fig. 5F** and **Fig. 5G**). Conversely, late neurons were enriched in the WT organoids. This observation was further highlighted by increased expression of neurogenesis-associated genes, such as NEUROD6 and NFIB, in both WOREE- and SCAR12-derived neurons as compared to WT (**Fig. S7A and Fig. S7B**). One possible interpretation of these results is that the observed differential maturity of transcriptional signatures might be a consequence of the earlier alterations in RG cells. Notably, only two genes were found to be differentially expressed between SCAR12 and WOREE neurons, suggesting that considerable differences in the manifestations of the diseases do not arise directly from the neuronal cells (**Supplementary Fig. 7C**).

Neuron-specific Gene Therapy Rescues Neuronal Hyperexcitability

We have previously shown that neuronal restoration of WWOX using an adeno-associated virus serotype 9 (AAV9), driven by Synapsin I promoter (*AAV9-SynapsinI-WWOX-2A-EGFP-WPRE*, referred to here as AAV9-WWOX) is able to rescue phenotypes seen in *Wwox*-null mice, including seizures, early lethality, and infertility (*56*). Given this remarkable success in *Wwox*-null mice, we set out to determine whether the molecular and electrophysiological phenotypes observed in the organoids could be rescued by neuronal AAV9-WWOX infection, irrespective of prior RG defects. To this end, we infected week 10 organoids with either AAV9-WWOX (see methods) or AAV9-EGFP (*AAV9-SynapsinI-EGFP-WPRE*), followed by 6 weeks of culture. We confirmed the success of infection in week 16 organoids by immunostaining (**Fig. 6A** and **Fig. S8**). Neuronal activity was then measured through Ca^{2+} imaging, revealing that the firing rate of WOREE organoids was approximately 3-fold higher than that of SCAR12 organoids (**Fig. 6B** and **S9**), in contrast to what we observed in an earlier time point, where both organoids showed similar neuronal hyperactivity (**Fig. 1B** and **Fig. 1C**). In both cases neuronal firing was significantly higher compared to the WT, with differences observed in event frequency, firing amplitude, and the proportion of active regions of interest (ROIs) in each organoid. Remarkably, neuron-specific restoration of WWOX was sufficient to reduce hyperexcitability to a level similar to the WT organoids (**Fig. 6B**).

Previously, we reported reduced SATB2 and CTIP2 expression (both by immunofluorescence and mRNA levels) in WWOX-KO and WOREE organoids (*21*). Therefore, we assessed if AAV9-WWOX infection could increase the expression of these markers. Immunostaining and qPCR analysis revealed again lower CTIP2 and SATB2 expression in WOREE organoids compared to the WT (**Fig. 6C-E** and **Fig. S10**). WWOX restoration increased the expression of both markers in WOREE organoids but not in SCAR12, which showed CTIP2 and SATB2 expression levels similar to WT. Next, to assess whether transcriptomic changes reflect our electrophysiological observations, we compared expression levels of neuronal cells from AAV9-WWOX treated WOREE organoids vs non-treated (**Fig. S6F-H**). AAV9-treated organoids showed changes in expression of mediators of neuronal activity, including reduced voltage-gated and ligand-gated ion channel expression and increased synaptic translation, together with an increase in genes involved in pathways suggestive of neuronal maturation, such as oxidative

phosphorylation (primary energy source for resting neuronal terminals and upregulated during cortical neuron differentiation) (*57–59*), promotion of oligodendrocyte differentiation and myelination, and synaptic function (**Fig. 6G** and **Fig. 6H**). Importantly, the infection with AAV9-WWOX of WOREE organoids did not affect the RGs, as appreciated by the absence of differentially expressed genes and cell-cycle abnormalities (**Fig. S11**), potentially pointing to the safety profile of this approach.

Discussion

In this study, we report insights into the cellular and molecular processes underlying WWOX-related neurological disorders. WOREE and SCAR12 syndromes are devastating diseases, yet due to their rarity, are rendered orphan. Our findings from the combination of iPSC-based models and omics analysis indicate that WWOX-deficient neural organoids exhibited reduced neurogenesis and an increased number of RGs, particularly in WWOX-deficient organoids. These RGs exhibited increased expression of MYC, verified in 2D-cultured NSCs, which could significantly influence brain development. Another major finding in our study was cell cycle alterations in WWOX-deficient RG cells, with cells accumulating in the G2/M and S phases. In addition, we provide evidence that neuronal WWOX restoration using an AAV9-based gene therapy could rescue hyperexcitability of patient-derived organoids.

Our earlier findings prompted the hypothesis that the complete loss of WWOX function disrupts corticogenesis. To rigorously investigate the implications of WWOX loss, we developed cerebral organoids completely lacking WWOX expression using CRISPR-edited and patient-derived iPSCs. This model was shown previously to effectively study the development and disease of NSCs within a human context (*60–62*). Given the high expression of WWOX in vRG cells, we anticipated that its loss would influence neuronal differentiation. Indeed, unbiased scRNA-seq revealed striking alterations in cellular populations, characterized by a marked increase in RG cells and a decrease in mature neurons. These findings further emphasize the pleiotropic functions of the WWOX gene (*4, 7*) and pose challenges in formulating potential therapeutic strategies.

The finding that WWOX-deficient RGs exhibit elevated Myc expression suggests a complex interplay between WWOX and Myc. The underlying mechanism of how WWOX affects Myc expression is yet to be determined. However, this increased Myc expression may influence cell cycle progression, a phenotype prominently observed in WWOX-mutant organoids. The implications of this relationship could significantly affect neuronal differentiation. Previous research using mouse embryonic cultures has demonstrated that elongation of the G1 phase during neurogenesis promotes neural progenitor differentiation, while a reduction in G1 duration inhibits neurogenesis and favors progenitor expansion (*63, 64*). WWOX was initially identified as a putative tumor suppressor in breast cancer, with the potential to influence cell growth (*65*). Therefore, our findings align closely with the expected functions of WWOX; however, our observations in a non-tumor context were previously unforeseen.

The activation of MYC can also result in genomic instability (*66, 67*), correlating with the increased DNA damage observed in a previous study (*21*). Elevated p53 levels in this context could suggest a compensatory response. While WWOX-deficient organoids demonstrated a reduction in differentiated neurons, this effect was less pronounced in patient-derived organoids, indicating a potentially detrimental process in which damaged RGs differentiate into neurons. Both MYC and p53 are known to impact cellular metabolism (*68, 69*), potentially affecting neuron maintenance and neurotransmitter production (*70, 71*), although these outcomes were not studied here.

MYC can also impact ribosome biogenesis and proliferation, as evident in mouse models, where interference with MYC led to a premature decrease in ribosome biogenesis and to neurodevelopmental deficits, such as macrocephaly (*72*). Conversely, high MYC expression enhanced protein biosynthesis and proliferation (*72*). During embryogenesis, MYC downregulation enables a metabolic shift from glycolysis to oxidative phosphorylation, which is crucial for neuroepithelial development (*73*). In proliferating neural progenitors, MYC, together with other transcription factors, activate the transcription of glycolytic genes such as HK2 and LDHA. In contrast, in neurons, MYC is downregulated allowing other transcription factors (such as PGC-1α and ERRγ) to take over and promote the expression of oxidative phosphorylation-related genes (*58*).

Our current study reveals improper activation of Wnt signaling in RGs from WWOX-deficient organoids, aligning with prior observations (Steinberg et al., 2021). Wnt is known to induce MYC expression in colorectal cancer and was shown to impact RG differentiation and stemness (*53, 74*). Consistent with our findings, dysregulation of the Wnt pathway in mouse RGs led to decreased RG proliferation and increased apoptosis (*75*). Specifically, activation of Wnt signaling at E10.5 inhibited cortical neural differentiation, while inactivation at E11 promoted terminal neurogenesis in neural progenitors (*76*). Furthermore, GSK-3β, a Wnt regulator inhibited by WWOX, plays a role in RG proliferation and differentiation. GSK-3β deletion resulted in hyperproliferation but also enhanced differentiation (*77, 78*). Our findings highlight the critical role of Wnt signaling dysregulation in WWOX-deficient organoids, which adversely affects RG proliferation and differentiation.

Our results reveal a broad phenotypic spectrum of WWOX-related neurological disorders, encompassing a continuum from mild to severe developmental epileptic encephalopathies. In addition to this phenotypic variability, our data facilitated a thorough analysis of genotype–phenotype correlations. Significantly, all neurons with WWOX mutations demonstrated hyperexcitability, providing the first evidence that SCAR12 organoids exhibit increased activity compared to baseline, although they are less active than neurons derived from WOREE patients. Furthermore, the neurons derived from patients displayed an "immature" gene expression profile—termed "early" due to the overall immaturity of the organoids—suggesting potential delayed differentiation.

We finally evaluated a neuron-specific gene therapy previously developed by our team, which had shown efficacy in *Wwox*-null mice (*56*). This therapy effectively normalized hyperexcitability in WOREE organoids and led to increased expression of neuronal

markers such as CTIP2 and SATB2. Additionally, pathways associated with neuronal maturation, including oxidative phosphorylation and synaptic ribosomal biogenesis, were upregulated, along with downregulation of voltage-gated ion channels, suggesting consistency with decreased electrophysiological phenotypes and a potential shift away from premature gene-expression signatures. Remarkably, this restoration also influenced myelination signaling, a function previously associated with WWOX deficiency in both mice and oligocortical spheroids (*24*).

Another potential therapeutic approach arising from our findings could involve silencing *MYC* in RGs. However, the pervasive role of *MYC* in essential cellular processes—ranging from chromatin organization and transcriptional regulation to cell cycle progression and metabolic programming—poses significant challenges for its manipulation during neurogenesis. For example, as highlighted earlier, *MYC* regulates key glycolytic genes critical for metabolic homeostasis during neurodevelopment, and its dysregulation has been linked to impaired differentiation and neuronal cell death (*58*). Furthermore, even as a proof-of-concept, modulating *MYC* could introduce considerable experimental variability and confounding effects, complicating the interpretation of results. That said, an intriguing avenue for future research would be to identify specific downstream targets of *MYC* that can be selectively modulated in *WWOX*-deficient RGs, potentially offering a more precise and less disruptive therapeutic strategy. Therefore, while targeting *MYC* represents an intriguing therapeutic concept, its central role in orchestrating diverse cellular functions necessitates careful evaluation of potential adverse consequences on neurodevelopment.

Collectively, our findings demonstrate that WWOX-mutations, associated with WOREE and SCAR12 syndromes, profoundly disrupt RG cell homeostasis and differentiation, and neuronal development, contributing to neurodevelopmental abnormalities. Our data suggest that these effects are driven, at least in part, by MYC overexpression and altered cell cycle dynamics, potentially regulated by Wnt signaling. In WWOX-deficient neural organoids, we observed hyperexcitability and delayed neuronal development. Notably, a neuron-specific gene therapy using AAV9-WWOX successfully rescued these deficits, normalizing hyperexcitability and promoting neuronal maturation. These results indicate that WWOX loss of function disrupts neurogenesis by dysregulating MYC, impairing neuronal differentiation and function. Our findings highlight the therapeutic potential of AAV9-WWOX in mitigating developmental deficits and highlight the important non-cell-autonomous role of WWOX in brain development.

Materials and Methods

Cell Culture and Maintenance

All iPSCs and hESCs (WiBR3) were maintained in 5% CO2 on irradiated DR4 mouse embryonic fibroblast (MEF) feeder layers. Cells were cultured in FGF-2/KOSR medium consisting of DMEM-F12 (Gibco; 21331-020 or Sartorius; 01-170-1A) supplemented with 15% Knockout Serum Replacement (KOSR, Gibco; 10828-028), 1% GlutaMax (Gibco; 35050-038), 1% MEM non-essential amino acids (NEAA, Sartorius; 01-340-1B), 1%

Sodium-pyruvate (Sartorius; 03-042-1B), 1% Penicillin-Streptomycin (Sartorius; 03-031-113), and 10 ng/mL bFGF (Peprotech; 100-18B). Medium was changed daily, and cultures were passaged every 5-7 days by TrypLE™ (Gibco; 12604013). Rho-associated kinase inhibitor (ROCKi, Y27632) (Cayman; 10005583) was added at 10 µM for the first 24-48 hours post-passaging.

For RNA or protein isolation, hPSCs were passaged onto Matrigel-coated plates (Corning; 356231) and cultured in NutriStem hPSC XF medium (Sartorius; 05-100-1A).

Transfection and Gene Editing

For transfection, iPSCs were pre-treated with 10 µM ROCKi for 24 hours. Cells were detached using TrypLE, resuspended in PBS (with Ca2+ and Mg2+), and mixed with 100 µg total DNA constructs. Electroporation was performed using the Gene Pulser Xcell System (Bio-Rad) at 250 V, 500 µF, in 0.4 cm cuvettes. Transfected cells were plated on MEF feeder layers in FGF/KOSR medium supplemented with ROCKi.

For WWOX Knockout, the px330 plasmid containing sgRNA targeting WWOX exon 1 was co-electroporated with pLKO.1 puro plasmid (1:10 ratio). After 48 hours, the cells were treated with puromycin at a X concentration for 72 hr, after which fresh medium was added. The cells were grown until distinct colonies appeared and were isolated for further expansion, after approximately 7 days. Gene editing was validated by Western blot. sgRNA sequence (*hWWOX*): 5′-CACCGCATGGCAGCGCTGCGCTACG-3′

Reprogramming of somatic cells

Skin biopsies and blood samples were obtained with informed consent under approval from the Kaplan Medical Center Helsinki committee.

Reprogramming was conducted using Sendai virus Cyto-Tune-iPS2.0 Kit according to manufacturer's instructions.

Peripheral blood mononuclear cells (PBMCs). PBMCs were isolated from a whole-blood sample obtained from a healthy adult male using ficoll gradient and cultured in StemPro-34™ medium supplemented with cytokines (SCF, FLT-3 ligand, IL-3, and IL-6). On day 0, cells were infected with reprogramming viruses. On day 3, cells were transferred to MEF-coated plates. By day 7, reprogramming cells were observed, and medium was gradually changed to mTeSR, supplemented with ROCKi for the first 48 hrs. On day 16, colonies were picked, expanded, validated for pluripotency markers, and sequenced for WWOX mutations. For further details, kindly refer to (*21*).

Skin fibroblasts. Primary fibroblasts obtained from donors were cultured in Fibroblast medium consisting of DMEM supplemented 15% Fetal Bovine Serum (FBS), 1% NEAA, 1% sodium pyruvate, 1% GlutaMax, 100 µM 2-mercaptoethanol without antibiotics. 2-4 days prior to reprogramming, the fibroblasts were seeded in 6-well plated coated with 2% gelatin solution and grown to 60-70% confluency. On day 0, cells were infected with Sendai viruses. The next day, the medium was replaced by fresh fibroblast medium. On days 2-6 the medium was changed daily. On day 7, fibroblasts were harvested using Trypsin type C solution (Sartorius; 03-053-1B) and seeded onto MEF-coated plates. On day 8, the medium was changed to FGF-2/KOSR medium as described above, with 10 µM ROCKi added for the first 3 days. The medium was replenished daily. By day 21, small

colonies appeared, and by day 28 the cells for colony picking and further expansion. All lines were stained and validated for pluripotency markers and sequenced for WWOX mutations.

All experiments conformed to the principles set out in the WMA Declaration of Helsinki and the Department of Health and Human Services Belmont Report.

Cerebral organoid generation and culture

Cerebral organoids were generated from iPSCs as previously described (*21*):

All iPSCs were maintained on mitotically inactivated MEFs. Prior to protocol initiation, cells were passaged onto 60mm plates coated with MEFs and grown to 70-80% confluency.

Embryoid Body (EB) Formation: On day 0, hESC colonies were dissociated to single cells using 1 mg/mL Dispase II solution (Sigma; D4693) followed by TrypLE treatment. 4,500 cells were seeded per well in ultra-low attachment 96-well U-bottom plates (S-Bio Prime; MS-9096UZ) in hESC medium (DMEM/F12, 20% KOSR, 1% GlutaMax, 1% NEAA, 1% Penicillin-Streptomycin, 100 µM 2-mercaptoethanol, 5 ng/mL bFGF, and 10 µM ROCKi). EBs were fed every other day for 5 days.

Neural Induction: On day 6, medium was replaced with Neural Induction (NI) medium (DMEM/F12, 1% N2 supplement, 1% GlutaMax, 1% MEM-NEAA, 1 µg/mL Heparin). NI medium was changed every other day until neuroepithelium establishment (days 11-12).

Matrigel Embedding and Differentiation: Well-developed EBs were embedded in Matrigel droplets and transferred to 90mm non-treated culture dishes with Cerebral Differentiation Medium (CDM: 1:1 DMEM/F12 and Neurobasal medium, 0.5% N2, 1% B27 without vitamin A, 1% GlutaMax, 1% penicillin/streptomycin, 0.5% NEAA, 50 µM 2-mercaptoethanol, 2.5 µg/mL insulin, and 3 µM CHIR-99021).

Maturation: From day 16, organoids were cultured on an orbital shaker in Cerebral Maturation Medium (CMM: DMEM/F12 and Neurobasal medium, 0.5% N2, 1% B27 with vitamin A, 1% GlutaMax, 1% penicillin/streptomycin, 0.5% NEAA, 50 µM 2-mercaptoethanol, 2.5 µg/mL insulin, 400 µM vitamin C, and 12.5 mM HEPES buffer, without CHIR-99021). From week 6, 1% Matrigel was added to the medium. Medium was changed every ≤ 72 hr, and organoids were transferred to fresh sterile plates every 30 days.

All of the described media were filtered through a 0.22µm filter and stored at 4°C until usage.

AAV9 infection

AAV9 viruses were obtained as described previously (*56*).

For infection, AVV9-WWOX and AAV9-EGFP viruses were diluted in CMM without antibiotics to a final concentration of $3x10^{10}$ GC/µL. The medium volume was calculated as 100 µL/organoid. Then, ~25 organoids at week 11 were transferred to low-attachment 6-well plates, the spent medium was carefully removed and 1.5 ml of virus-containing CMM was added. The organoids were cultured stationary for 5 hr in a humidified incubator, followed by the addition of extra 1.5 ml of virus containing medium was added

before over-night incubation. The following morning, the medium was diluted 1:1 with fresh CMM and the organoids were incubated for an additional 24 hr. After ~48 hr after the original infection, a complete medium change was performed and the organoids were cultured as described in an earlier section, up until harvesting for analysis at week 16.

NSCs differentiation

Neural stem cells (NSCs) were generated from hESCs using a modified dual-SMAD inhibition protocol (*42*). Briefly, WiBR3 hESCs cultured on a MEF-feeder layer were released from MEFs and dissociated to single cells as previously described for organoids, and seeded on Matrigel-coated plates at 50,000 cells/cm^2 in MEF-conditioned media supplemented with 10 ng/mL FGF-2 and 10 μM ROCKi. Neural induction was initiated the following day using a NSCs medium containing DMEM/F12:Neurobasal (1:1), 2% B27 supplement, 1% N2 supplement, 1% Penicillin-Streptomycin, 1% NEAA and 100 μM β-mercaptoethanol. From day 1 to 10, dual SMAD inhibitors 100 nM LDN-193189 (Axon Medchem; 1527) and 20 μM SB-431542 (Sigma; S4317) were added along with 1 μM XAV-939 (Peprotech; 2848932). From day 10 to 20, SMAD inhibitors were withdrawn, and 50 nM SAG (Sigma; 566660) was added with 1 μM XAV-939. The medium was changed daily. By day 20-22, cells had become NSCs, were passaged and cryopreserved, and marker expression was validated using immunofluorescence.
NSCs were maintined on Matrigel-coated plates in NSCs medium supplemented with N2 (1%), B27 (2%), 40 ng/ml EGF (Peprotech; AF-100-15), 40 ng/ml FGF2, and 1.5 ng/mL hLIF (Sigma; L5283). Medium was changed every 2-3 days, and cells were passaged at 60-70% confluence using TripLE at room temperature.

Immunofluorescence

Organoids fixation and immunostaining were performed as previously described (*21*). Briefly, for histological analysis, organoids were rinsed thrice in PBS before being immersed in 4% ice-cold paraformaldehyde for 45 minutes on an orbital shaker for fixation. Following three cold PBS washes, the organoids were subjected to cryoprotection by overnight immersion in a 30% sucrose solution. Subsequently, the organoids were embedded in OCT compound, rapidly frozen on dry ice, and sectioned at 10 μm thickness using Leica CM1950 cryostats.
Immunofluorescent staining was performed on these sections following a standard procedure. First, they were brought to room temperature and rehydrated in PBS. The sections were then permeabilized using 0.1% Triton X in PBS (PBT) and blocked for 60 minutes in a solution containing 5% normal goat serum (NGS) and 0.5% BSA in PBT. Primary antibodies, diluted in the blocking solution, were applied to the sections and incubated overnight at 4°C. The following day, the sections were washed three times in PBS with 0.05% Tween-20 (PBST) under gentle agitation on an orbital shaker. Secondary antibodies and Hoechst33258, diluted in blocking buffer, were then applied for 90 minutes. After four PBST washes while place on an orbital shaker, coverslips were mounted using Immunofluorescence Mounting Medium (Dako; s3023). An Olympus FLUOVIEW FV1000 confocal laser scanning microscope was used for imaging, with image processing carried out using the associated Olympus FLUOVIEW software or NIH

ImageJ. Quantification of marker-positive cells was conducted using QuPath v0.5.1, followed by statistical analysis as described in later sections.
List of primary and secondary antibodies used in this work, together with dilution details can be found in Table S1.

Cell-attached recordings

Cell-attached recordings was performed as previously described (*21*), briefly: Spontaneous neuronal activity from organoid neuronal populations was recorded using blind patch-clamp techniques. Glass electrodes (approximately 7 MOhm resistance) were fabricated from filamented, thin-walled borosilicate glass (1.5 mm outer diameter, 0.86 mm inner diameter; Hilgenberg GmbH, Malsfeld, Germany) using a vertical two-stage puller (PC-12, Narishige, East Meadow, NY). The electrodes were filled with an internal solution comprising (in mM): 140 K-gluconate, 10 KCl, 10 HEPES, 10 Na2-Phosphocreatine, 0.5 EGTA, adjusted to pH 7.25 with KOH.
Electrodes were inserted at a 45° angle relative to the organoid surface. During recordings, organoids were maintained in Cerebral Maturation Medium (CMM) without Matrigel at 35°C. An increase in pipette resistance to 10-200 MOhm typically coincided with the appearance of spikes, which served as the criterion to initiate recording. All recordings were acquired using an intracellular amplifier in current-clamp mode (Multiclamp 700B, Molecular Devices), sampled at 10 kHz (CED Micro 1401-3, Cambridge Electronic Design Limited), and filtered with a high-pass filter to isolate neuronal spikes from field potentials.
Analysis of cell-attached recordings was performed using custom-written MATLAB code. Spikes were extracted from raw voltage traces by applying a threshold set well above the background noise level. The average firing rate for each recorded cell was calculated over a 4-minute recording period.

Ca2+ Imaging

Calcium imaging was performed for neural organoids at 16 weeks post-differentiation. In brief, Calcium transients were observed by incubating cerebral organoids for an hour with 8 µM Fluo-5 AM (Abcam; ab241083) in the ACSF, i.e., recording solution containing (in mM) 139 NaCl, 10 HEPES, 4 KCl, 2 CaCl2, 10 D-glucose, and 1 MgCl2 (pH 7.5, osmolarity adjusted to 310 mOsm). After one hour of incubation, the organoids were placed in a recording chamber filled with clean ACSF that had been pre-warmed to 37 °C, and imaging of calcium transients was performed on a SliceScope Pro 3000 microscope (Scientifica) with a CCD digital camera (Scientifica, SciCam Pro). The images and data were captured and processed using a custom-written GUI in MATLAB 9.8 (R2021a, MathWorks). Recording of single cells were performed at an acquisition rate of 10 Hz. Time series data of calcium imaging recordings was analyzed using a custom-written Python script. The intensity of shifts in fluorescence levels was calculated by measuring the changes between the values of two adjacent image frames. The fluorescence ratio ($\Delta f/f0$) was calculated by dividing the signal's maximum amplitude by the baseline fluorescence which was calculated as the average signal when the cell was inactive.

Immunoblot analysis

Organoids homogenized in lysis buffer containing 50 mM Tris (pH 7.5),150 mM NaCl, 10% glycerol, and 0.5% Nonidet P-40 (NP-40) that was supplemented with protease and phosphatase inhibitors and incubated on ice for 15 minutes. The samples were than centrifuged, and liquid phase was collected.

Western blotting was performed under standard conditions, with 30-50 µg protein used for each sample. Blots were repeated and quantified 2–3 times per experiment in Bio-Rad's Image Lab software. Representative images of those repeated experiments are shown.

RNA extraction, reverse transcription-PCR, and qPCR

Total RNA was isolated using Bio-Tri reagent (Biolab; 9010233100) and cleaned using the Zymo Direct-zol RNA MiniPrep kit (Zymo; R2050) as described by the manufacturer. 0.25-1 µg of RNA was used to synthesize cDNA using a qScript cDNA Synthesis kit (QuantaBio; 95047). qRT-PCR was performed using Power SYBR Green PCR Master Mix (Applied Biosystems; AB4367659). All measurements were performed in triplicate and were standardized to the levels of either HPRT or UBC. All primer sequence used are noted in Table S2.

Library preparation and Single-cell RNA-seq (scRNA-seq) (10x Chromium)

Neural organoids were dissociated into single cells papain-based enzymatic digestion method, based on a previously published protocol (*33*), with the following variations: 3-4 organoids from each hPSCs line were transferred to a 60 mm culture dish containing 4 mL of pre-warmed Earle's Balanced Salt Solution (EBSS) (Sartorius; 02-010-1A). The organoids were manually dissected into small pieces and transferred into a new 60 mm dish containing 2.5 mL of Enzymatic dissociation solution [composed of 27.3 U/mL papain solution (Worthington; LS003126) supplemented with 200 U/mL of DNase I solution (Sigma; 10104159001) and 10 µM ROCKi in Hanks' Balanced Salt Solution (HBSS) (Sartorius; 02-015-1A)], and incubated on a shaker (70 rpm) in a humidified incubator for 30 minutes at 37°C.

Following digestion, the tissue was collected in a 15 mL tube, and 5 mL of warm EBSS was added. The mixture was triturated 20 times using a 10 mL pipette, after which it was allowed to settle until all pieces sank. The resulting supernatant containing dissociated cell suspension was carefully transferred to a new 15 mL tube, avoiding any undigested tissue pieces. To the cell suspension, 5 mL of EBSS, 3 mL of Enzyme inhibiting solution [containing 10 mg/mL Trypsin inhibitor solution (Sigma; T9253) and 10 mg/mL BSA in EBSS) were added and gently mixed. Cells were pelleted by centrifugation at 300 g for 7 minutes at room temperature. The liquid was aspirated, and 5 ml of warm EBSS was added, the cells were centrifuged again and resuspended in cold 0.1% BSA solution + 10 µM ROCKi in PBS. The cells were passed through a 40 µm strainer. Cell viability and concentration were determined using trypan blue staining. Finally, cells were diluted in ice-cold DPBS + 0.1% BSA + ROCKi solution to a concentration of 100 cells/µL and kept on ice until droplet collection.

Library preparation and sequencing was done by the Hebrew University's Core facility following a standard protocol. Briefly, single-cell suspensions, prepared as described in

the previous section, were processed for RNA sequencing using the 10x Genomics platform. Libraries were generated using the Chromium Next GEM Single Cell 3 GEM, Library & Gel Bead Kit v3.1 (10× Genomics, Pleasanton, CA, USA), following the manufacturer's protocol. Libraries that had passed quality control were then sequenced on an Illumina NovaSeq 6000 platform (Illumina, San Diego, CA, USA). Sequencing parameters were set to generate paired-end reads with the following specifications: 28 base pairs (bp) for Read 1 and 90 bp for Read 2. Read 1 contained cell-identifying barcodes and unique molecular identifiers (UMIs), while Read 2 corresponded to mRNA transcript sequences. The sequencing depth was targeted to achieve approximately 50,000 reads per cell, overall obtaining about 1B reads, which were evenly distributed between the 5 libraries.

Single-cell data preprocessing

Organoids from five different conditions (WT = 6,792; WWOX-KO = 4,124; SCAR12 = 4,454; WOREE = 7,687; WOREEWWOX = 5,151) were analyzed jointly, resulting in a total of 28,208 cells. After removing undetected genes and cells with high mitochondrial content or total count numbers, we retained 26,352 high-quality cells.

Normalization, batch correction, clustering, dimensionality reduction, and visualization steps were performed using the computational tool ACTIONet (*79*), release version available at (https://github.com/shmohammadi86/ACTIONet/tree/R-release). Batch effects were corrected using Harmony accounting for the condition of the organoids. Clusters were identified using the Leiden algorithm with default parameters implemented in ACTIONet. 12 cell clusters were annotated based on manually curated marker genes and transcriptional signature comparisons with a human primary single-cell data covering early (*37*), mid (*34, 36*), and late (*35*) fetal cortical development. Cluster profiles were generated as the average expression across cells within each cluster. Signatures were calculated using the total pairwise fold-change sum of a given cluster profile relative to others. Statistical overrepresentation analyses of marker genes manually curated from the literature on these signatures were used to interpret and annotate the clusters. Correlation of cluster signatures with cell type signatures from single-cell data from the primary samples was used to further support cluster annotations. Clusters that could not be confidently mapped to specific cell types and/or presented offset differentiation or stress signatures were flagged and not considered for downstream analyses. A total of 18,007 cells annotated as radial glia, neuronal progenitors, or neurons (WT = 5,649; WWOX-KO = 3,020; SCAR12 = 3,422; WOREE = 5,916; $\text{WOREE}_{\text{WWOX}}$ = 3,763) passed all quality controls.

Differential Gene Expression

Differential gene expression (DGE) analysis was performed using nonparametric Wilcoxon tests as implemented in the R package *presto* (*80*). Genes with a log fold change of ±0.5 and a p-value < 0.05 were considered differential. DGE analysis was performed separately for radial glia cells and for neuronal progenitor and neuronal cells.

WWOX and MYC expression in vivo

Human single-cell data at post-conceptional week 16 (*36*) and tissue-level cell sorted data from week 13 to 20 (*39*) were used to asses WWOX gene expression in vivo. Expression at single-cell level was assessed by projecting WWOX expression onto a 2D manifold of the data using the uniform manifold approximation method (UMAP) as implemented in ACTIONet. The same approach was applied to visualize radial glia (VIM, SOX2), and neuronal (TBR1, SATB2, NEUROD6) markers for comparison. Expression values at single-cell level were further compared and correlated with annotated cell types. Expression in FACS-sorted data was assessed by comparing relative expression values of WWOX across fetal cell types. Expression in tissue-level data was assessed across either developmental time or anatomical zones. Temporal expression of WWOX and MYC was assessed in human forebrain developmental data from embryonic stages to adulthood (*40*) and in reference time-series of cortical organoid differentiation (*9*). Observed trends are based on smoothed normalized expression estimated using Tukey's methods as implemented in the *smooth* function from the stats package in R. Anatomical zone expression was assessed in laser microdissected human fetal data (*38*). Relative expression values are based on mean- subtracted values across all cortical zones. Log-transformed TMM normalization as implemented in the R package *edgeR* (*82*) was used to account for library size variation. Replicates were averaged only for samples between days 25 and 463 of differentiation. All heatmap visualizations were performed using the R package *Complex Heatmap* (*81*).

Cell cycle phase and potency state inference

To estimate the cell cycle phase of radial glia cells from single-cell transcriptomic data, the *tricycle* R package (*47, 82*) was used with default parameters. The cell phase discretization was defined based on the cell cycle timepoint of each single cell as follows: G1/G0 0π - 0.5π and > 2π, S 0.5π - 1π, G2M 1π - 1.5π, M 1.5π - 2π. The cell cycle proportions between WWOX-KO and WT were compared by calculating the proportion of cells in each phase relative to the total number of cells in each condition and by computing the log2 fold change between WWOX-KO and WT conditions. To assess the prevalence of MYC expression across cell cycle phases, gene expression levels were correlated to the cell cycle phase estimations and the contribution for each condition was estimated. The potency potential os single cells was estimated from transcriptomic data using the CytoTrace2 package as described in (*52*). Cells were categorized into three potency levels: Multipotent (high potency), Oligopotent/Unipotent (medium potency), and Differentiated (low potency).

Overrepresentation analysis

Statistical overrepresentation estimations of conditions and cell cycle phases across potency states in radial glia cells are based on binomial tests on the 3 potency categories.

Enrichment analysis of pathways of interest obtained from the *EnrichR* database (https://maayanlab.cloud/Enrichr/#libraries), KEGG, and REACTOME databases, was assessed on ranked transcriptional signatures of potency states by using the assess.geneset.enrichment.from.scores function of the ACTIONet package. MYC positive

and negative regulon genesets were obtained from an integrative database for the estimation of human transcription factor activities (*VIPER*) (*83*). The p-values were adjusted using Bonferroni correction, and all scores calculated as -log10 (p-value) were capped to a maximum value of 10 for visualization purposes. Gene Set Enrichment Analysis (GSEA) was performed over ranked scores using the *fgsea* R package (*84*). The pathway database *SynGO* (*85*) was used to estimate enrichment over log2 fold changes between experimental conditions in neuronal cells.

Neuron Analysis

Neurons and intermediate progenitors from all conditions were isolated and re-analyzed following the ACTIONet standard pipeline described above. To interpret neuronal subtypes, reference neuronal cell type-specific signatures were computed from (*55*) and correlated to the organoid cluster signatures. Neuron clusters were interpreted and annotated based on reference correlations and preferential expression of marker genes. For clusters expressing markers associated with both excitatory and inhibitory neurons and showing ambiguous mapping in the correlation matrix, a "mixed neurons" category was assigned. The resulting 7 subtypes were divided into early excitatory neurons (EN-IT Immature, EN Newborn, and IPC-EN) and late excitatory neurons (EN-L5-ET, EN-L5-CT, EN-L6-CT, and Mixed Neurons).

Pseudobulk analysis

All pseudobulk profiled were estimated from the single-cell data as the sum of raw counts over cells of a given condition and normalized as log-transformed counts per million (cpm).

Statistical analysis

Results of the experiments were expressed as mean ± SEM. Statistical significance was determined either by using one-way ANOVA was, correcting for the multiple comparisons with Tukey's multiple comparisons test, or by using multiple t-tests, correcting for multiple comparisons by controlling the False Discovery Rate (FDR) using the Benjamini–Hochberg procedure. The specific test used in each experiment is described in the corresponding Fig. legend. *P*-value cutoff for statistically significant results were used as following: n.s (non-significant), *$p \leq 0.05$, **$p \leq 0.01$, ***$p \leq 0.001$, ****$p \leq 0.0001$. Statistical analysis and visual data presentation were preformed using GraphPad Prism 9. No randomization or blinding was applied in this study. The experiments were performed on several biological replicates, with at least two clones of each hPSC lines used for each genotype (except for the WiBR3 WT and JH-iPS11 WT lines).

References

1. G. Abdel-Salam, M. Thoenes, H. H. Afifi, F. Körber, D. Swan, H. J. Bolz, The supposed tumor suppressor gene WWOX is mutated in an early lethal microcephaly syndrome with epilepsy, growth retardation and retinal degeneration. *Orphanet Journal of Rare Diseases* **9**, 12 (2014).

2. M. Mallaret, M. Synofzik, J. Lee, C. A. Sagum, M. Mahajnah, R. Sharkia, N. Drouot, M. Renaud, F. A. C. Klein, M. Anheim, C. Tranchant, C. Mignot, J.-L. Mandel, M. Bedford, P. Bauer, M. A. Salih, R. Schüle, L. Schöls, C. M. Aldaz, M. Koenig, The tumour suppressor gene WWOX is mutated in autosomal recessive cerebellar ataxia with epilepsy and mental retardation. *Brain* **137**, 411–419 (2014).

3. C. Mignot, L. Lambert, L. Pasquier, T. Bienvenu, A. Delahaye-Duriez, B. Keren, J. Lefranc, A. Saunier, L. Allou, V. Roth, M. Valduga, A. Moustaïne, S. Auvin, C. Barrey, S. Chantot-Bastaraud, N. Lebrun, M. L. Moutard, M. C. Nougues, A. I. Vermersch, B. Héron, E. Pipiras, D. Héron, L. Olivier-Faivre, J. L. Guéant, P. Jonveaux, C. Philippe, WWOX-related encephalopathies: Delineation of the phenotypical spectrum and emerging genotype-phenotype correlation. *Journal of Medical Genetics* **52**, 61–70 (2015).

4. E. Banne, B. Abudiab, S. Abu-Swai, S. R. Repudi, D. J. Steinberg, D. Shatleh, S. Alshammery, L. Lisowski, W. Gold, P. L. Carlen, R. I. Aqeilan, Neurological Disorders Associated with WWOX Germline Mutations—A Comprehensive Overview. *Cells* **10**, 824 (2021).

5. J. Piard, L. Hawkes, M. Milh, L. Villard, R. Borgatti, R. Romaniello, M. Fradin, Y. Capri, D. Héron, M.-C. Nougues, C. Nava, O. T. Arsene, D. Shears, J. J. C. Taylor, A. Pagnamenta, J. J. C. Taylor, Y. Sogawa, D. Johnson, H. Firth, P. Vasudevan, G. Jones, M.-A. Nguyen-Morel, T. Busa, A. Roubertie, M. van den Born, E. Brischoux-Boucher, M. Koenig, C. Mignot, U. Kini, C. Philippe, D. D. D. Study, The phenotypic spectrum of WWOX-related disorders: 20 additionalcases of WOREE syndrome and review of the literature. *Genetics in Medicine* **21**, 1308–1318 (2019).

6. K. L. Oliver, M. Trivisano, S. A. Mandelstam, A. De Dominicis, D. I. Francis, T. E. Green, A. M. Muir, A. Chowdhary, C. Hertzberg, K. Goldhahn, J. Metreau, C. Prager, J. Pinner, M. Cardamone, K. A. Myers, R. J. Leventer, G. Lesca, M. Bahlo, M. S. Hildebrand, H. C. Mefford, A. M. Kaindl, N. Specchio, I. E. Scheffer, WWOX developmental and epileptic encephalopathy: Understanding the epileptology and the mortality risk. *Epilepsia* **64**, 1351–1367 (2023).

7. M. Abu-Remaileh, E. Joy-Dodson, O. Schueler-Furman, R. I. Aqeilan, Pleiotropic functions of tumor suppressor WWOX in normal and cancer cells. *Journal of Biological Chemistry* **290**, 30728–30735 (2015).

8. C. M. Aldaz, T. Hussain, WWOX Loss of Function in Neurodevelopmental and Neurodegenerative Disorders. *International Journal of Molecular Sciences* **21**, 8922 (2020).

9. A. Gordon, S.-J. Yoon, S. S. Tran, C. D. Makinson, J. Y. Park, J. Andersen, A. M. Valencia, S. Horvath, X. Xiao, J. R. Huguenard, S. P. Pa□ca, D. H. Geschwind, Long-term maturation of human cortical organoids matches key early postnatal transitions. *Nature Neuroscience 2021 24:3* **24**, 331–342 (2021).

10. G. C. Schoenwolf, S. B. Bleyl, P. R. Brauer, P. H. Francis-West, “Third Week: Becoming Trilaminar and Establishing Body Axes” in *Larsen’s Human Embryology* (Elsevier, 2020), pp. 55–77.

11. M. G. Andrews, L. Subramanian, J. Salma, A. R. Kriegstein, How mechanisms of stem cell polarity shape the human cerebral cortex. *Nature Reviews Neuroscience* **23**, 711–724 (2022).

12. M. Götz, W. B. Huttner, The cell biology of neurogenesis. *Nature Reviews Molecular Cell Biology* **6**, 777–788 (2005).

13. A. R. Kriegstein, L. Subramanian, K. Obernier, A. Alvarez-Buylla, “Neural stem cells among glia” in *Patterning and Cell Type Specification in the Developing CNS and PNS* (Elsevier, 2020), pp. 775–806.

14. J. H. Lui, D. V. Hansen, A. R. Kriegstein, Development and Evolution of the Human Neocortex. *Cell* **146**, 18–36 (2011).

15. M. S. Zarzor, I. Blumcke, S. Budday, Exploring the role of the outer subventricular zone during cortical folding through a physics-based model. *eLife* **12** (2023).

16. D. V. Hansen, J. H. Lui, P. R. L. Parker, A. R. Kriegstein, Neurogenic radial glia in the outer subventricular zone of human neocortex. *Nature* **464**, 554–561 (2010).

17. B. E. LaMonica, J. H. Lui, D. V. Hansen, A. R. Kriegstein, Mitotic spindle orientation predicts outer radial glial cell generation in human neocortex. *Nature Communications* **4**, 1665 (2013).

18. A. A. Pollen, T. J. Nowakowski, J. Chen, H. Retallack, C. Sandoval-Espinosa, C. R. Nicholas, J. Shuga, S. J. Liu, M. C. Oldham, A. Diaz, D. A. Lim, A. A. Leyrat, J. A. West, A. R. Kriegstein, Molecular Identity of Human Outer Radial Glia during Cortical Development. *Cell* **163**, 55–67 (2015).

19. E. Taverna, M. Götz, W. B. Huttner, The Cell Biology of Neurogenesis: Toward an Understanding of the Development and Evolution of the Neocortex. *Annual Review of Cell and Developmental Biology* **30**, 465–502 (2014).

20. T. J. Nowakowski, A. A. Pollen, C. Sandoval-Espinosa, A. R. Kriegstein, Transformation of the Radial Glia Scaffold Demarcates Two Stages of Human Cerebral Cortex Development. *Neuron* **91**, 1219–1227 (2016).

21. D. J. Steinberg, S. Repudi, A. Saleem, I. Kustanovich, S. Viukov, B. Abudiab, E. Banne, M. Mahajnah, J. H. Hanna, S. Stern, P. L. Carlen, R. I. Aqeilan, Modeling genetic epileptic encephalopathies using brain organoids. *EMBO Molecular Medicine* **13**, e13610 (2021).

22. P. Arlotta, Organoids required! A new path to understanding human brain development and disease. *Nature Methods* **15**, 27–29 (2018).

23. Q. Yang, Y. Hong, T. Zhao, H. Song, G. Ming, What Makes Organoids Good Models of Human Neurogenesis? *Front. Neurosci.* **16**, 872794 (2022).

24. S. Repudi, D. J. Steinberg, N. Elazar, V. L. Breton, M. S. Aquilino, A. Saleem, S. Abu-Swai, A. Vainshtein, Y. Eshed-Eisenbach, B. Vijayaragavan, O. Behar, J. J. Hanna, E. Peles, P. L. Carlen, R. I. Aqeilan, Neuronal deletion of Wwox , associated with WOREE syndrome, causes epilepsy and myelin defects. *Brain*, doi: 10.1093/brain/awab174 (2021).

25. S. P. Pa□ca, P. Arlotta, H. S. Bateup, J. G. Camp, S. Cappello, F. H. Gage, J. A. Knoblich, A. R. Kriegstein, M. A. Lancaster, G.-L. Ming, A. R. Muotri, I.-H. Park, O. Reiner, H. Song, L. Studer, S. Temple, G. Testa, B. Treutlein, F. M. Vaccarino, A nomenclature consensus for nervous system organoids and assembloids. *Nature* **609**, 907–910 (2022).

26. T. Hussain, K. Sanchez, J. Crayton, D. Saha, C. Jeter, Y. Lu, M. Abba, R. Seo, J. L. Noebels, L. Fonken, C. M. Aldaz, WWOX P47T partial loss-of-function mutation induces epilepsy, progressive neuroinflammation, and cerebellar degeneration in mice phenocopying human SCAR12. *Progress in Neurobiology* **223**, 102425–102425 (2023).

27. M. A. Lancaster, M. Renner, C. A. Martin, D. Wenzel, L. S. Bicknell, M. E. Hurles, T. Homfray, J. M. Penninger, A. P. Jackson, J. A. Knoblich, Cerebral organoids model human brain development and microcephaly. *Nature* **501**, 373–379 (2013).

28. E. A. Alcamo, L. Chirivella, M. Dautzenberg, G. Dobreva, I. Fariñas, R. Grosschedl, S. K. McConnell, Satb2 Regulates Callosal Projection Neuron Identity in the Developing Cerebral Cortex. *Neuron* **57**, 364–377 (2008).

29. O. Britanova, C. de Juan Romero, A. Cheung, K. Y. Kwan, M. Schwark, A. Gyorgy, T. Vogel, S. Akopov, M. Mitkovski, D. Agoston, N. Šestan, Z. Molnár, V. Tarabykin, Satb2 Is a Postmitotic Determinant for Upper-Layer Neuron Specification in the Neocortex. *Neuron* **57**, 378–392 (2008).

30. D. P. Leone, W. E. Heavner, E. A. Ferenczi, G. Dobreva, J. R. Huguenard, R. Grosschedl, S. K. McConnell, Satb2 Regulates the Differentiation of Both Callosal and Subcerebral Projection Neurons in the Developing Cerebral Cortex. *Cerebral Cortex* **25**, 3406–3419 (2015).

31. W. L. McKenna, C. F. Ortiz-Londono, T. K. Mathew, K. Hoang, S. Katzman, B. Chen, Mutual regulation between Satb2 and Fezf2 promotes subcerebral projection neuron identity in the developing cerebral cortex. *Proceedings of the National Academy of Sciences* **112**, 11702–11707 (2015).

32. S. J. Pradhan, P. C. Reddy, M. Smutny, A. Sharma, K. Sako, M. S. Oak, R. Shah, M. Pal, O. Deshpande, G. Dsilva, Y. Tang, R. Mishra, G. Deshpande, A. J. Giraldez, M. Sonawane, C.-P. Heisenberg, S. Galande, Satb2 acts as a gatekeeper for major developmental transitions during early vertebrate embryogenesis. *Nature Communications* **12**, 6094–6094 (2021).

33. S. Velasco, B. Paulsen, P. Arlotta, Highly reproducible human brain organoids recapitulate cerebral cortex cellular diversity. *Protocol Exchange* (2019).

34. D. Polioudakis, L. de la Torre-Ubieta, J. Langerman, A. G. Elkins, X. Shi, J. L. Stein, C. K. Vuong, S. Nichterwitz, M. Gevorgian, C. K. Opland, D. Lu, W. Connell, E. K. Ruzzo, J. K. Lowe, T. Hadzic, F. I. Hinz, S. Sabri, W. E. Lowry, M. B. Gerstein, K. Plath, D. H. Geschwind, A Single-Cell Transcriptomic Atlas of Human Neocortical Development during Mid-gestation. *Neuron* **103**, 785-801.e8 (2019).

35. S. I. Ramos, Z. M. Mussa, E. N. Falk, B. Pai, B. Giotti, K. Allette, P. Cai, F. Dekio, R. Sebra, K. G. Beaumont, A. M. Tsankov, N. M. Tsankova, An atlas of late prenatal human neurodevelopment resolved by single-nucleus transcriptomics. *Nature Communications* **13**, 7671–7671 (2022).

36. A. E. Trevino, F. Müller, J. Andersen, L. Sundaram, A. Kathiria, A. Shcherbina, K. Farh, H. Y. Chang, A. M. Pa□ca, A. Kundaje, S. P. Pa□ca, W. J. Greenleaf, Chromatin and gene-regulatory dynamics of the developing human cerebral cortex at single-cell resolution. *Cell* **184**, 5053-5069.e23 (2021).

37. D. van Bruggen, F. Pohl, C. M. Langseth, P. Kukanja, H. Lee, A. M. Albiach, M. Kabbe, M. Meijer, S. Linnarsson, M. M. Hilscher, M. Nilsson, E. Sundström, G. Castelo-Branco, Developmental landscape of human forebrain at a single-cell level identifies early waves of oligodendrogenesis. *Developmental Cell* **57**, 1421-1436.e5 (2022).

38. J. A. Miller, S.-L. Ding, S. M. Sunkin, K. A. Smith, L. Ng, A. Szafer, A. Ebbert, Z. L. Riley, J. J. Royall, K. Aiona, J. M. Arnold, C. Bennet, D. Bertagnolli, K. Brouner, S. Butler, S. Caldejon, A. Carey, C. Cuhaciyan, R. A. Dalley, N. Dee, T. A. Dolbeare, B. A. C. Facer, D. Feng, T. P. Fliss, G. Gee, J. Goldy, L. Gourley, B. W. Gregor, G. Gu, R. E. Howard, J. M. Jochim, C. L. Kuan, C. Lau, C.-K. Lee, F. Lee, T. A. Lemon, P. Lesnar, B. McMurray, N. Mastan, N. Mosqueda, T. Naluai-Cecchini, N.-K. Ngo, J. Nyhus, A. Oldre, E. Olson, J. Parente, P. D. Parker, S. E. Parry, A. Stevens, M. Pletikos, M. Reding, K. Roll, D. Sandman, M. Sarreal, S. Shapouri, N. V. Shapovalova, E. H. Shen, N. Sjoquist, C. R. Slaughterbeck, M. Smith, A. J. Sodt, D. Williams, L. Zöllei, B. Fischl, M. B. Gerstein, D. H. Geschwind, I. A. Glass, M. J. Hawrylycz, R. F. Hevner, H. Huang, A. R. Jones, J. A. Knowles, P. Levitt, J. W. Phillips, N. Šestan, P. Wohnoutka, C. Dang, A. Bernard, J. G. Hohmann, E. S. Lein, Transcriptional landscape of the prenatal human brain. *Nature* **508**, 199–206 (2014).

39. M. Song, M.-P. Pebworth, X. Yang, A. Abnousi, C. Fan, J. Wen, J. D. Rosen, M. N. K. Choudhary, X. Cui, I. R. Jones, S. Bergenholtz, U. C. Eze, I. Juric, B. Li, L. Maliskova, J. Lee, W. Liu, A. A. Pollen, Y. Li, T. Wang, M. Hu, A. R. Kriegstein, Y. Shen, Cell-type-specific 3D epigenomes in the developing human cortex. *Nature* **587**, 644–649 (2020).

40. M. Cardoso-Moreira, J. Halbert, D. Valloton, B. Velten, C. Chen, Y. Shao, A. Liechti, K. Ascenção, C. Rummel, S. Ovchinnikova, P. V. Mazin, I. Xenarios, K. Harshman, M. Mort, D. N. Cooper, C. Sandi, M. J. Soares, P. G. Ferreira, S. Afonso, M. Carneiro, J. M. A. Turner, J. L. VandeBerg, A. Fallahshahroudi, P. Jensen, R. Behr, S. Lisgo, S. Lindsay, P. Khaitovich, W. Huber, J. Baker, S. Anders, Y. E. Zhang, H. Kaessmann, Gene expression across mammalian organ development. *Nature* **571**, 505–509 (2019).

41. R. Akkawi, O. Hidmi, A. Haj-Yahia, J. Monin, J. Diment, Y. Drier, G. S. Stein, R. I. Aqeilan, WWOX promotes osteosarcoma development via upregulation of Myc. *Cell Death & Disease* **15**, 13–13 (2024).

42. D. Cohen-Carmon, M. Sorek, V. Lerner, M. S. Divya, M. Nissim-Rafinia, Y. Yarom, E. Meshorer, Progerin-Induced Transcriptional Changes in Huntington's Disease Human Pluripotent Stem Cell-Derived Neurons. *Molecular Neurobiology* **57**, 1768–1777 (2020).

43. S. E. Ahmadi, S. Rahimi, B. Zarandi, R. Chegeni, M. Safa, MYC: a multipurpose oncogene with prognostic and therapeutic implications in blood malignancies. *Journal of Hematology & Oncology* **14**, 121–121 (2021).

44. D. W. Felsher, A. Zetterberg, J. Zhu, T. Tlsty, J. M. Bishop, Overexpression of MYC causes p53-dependent G2 arrest of normal fibroblasts. *Proceedings of the National Academy of Sciences* **97**, 10544–10548 (2000).

45. L. García-Gutiérrez, M. D. Delgado, J. León, MYC Oncogene Contributions to Release of Cell Cycle Brakes. *Genes* **10**, 244–244 (2019).

46. M. Schuhmacher, D. Eick, Dose-dependent regulation of target gene expression and cell proliferation by c-Myc levels. *Transcription* **4**, 192–197 (2013).

47. S. C. Zheng, G. Stein-O'Brien, J. J. Augustin, J. Slosberg, G. A. Carosso, B. Winer, G. Shin, H. T. Bjornsson, L. A. Goff, K. D. Hansen, Universal prediction of cell-cycle position using transfer learning. *Genome Biology* **23**, 41–41 (2022).

48. D. Deb-Basu, Å. Karlsson, Q. Li, C. V. Dang, D. W. Felsher, MYC Can Enforce Cell Cycle Transit from G1 to S and G2 to S, But not Mitotic Cellular Division, Independent of p27 Inhibition of Cyclin E/CDK2. *Cell Cycle* **5**, 1348–1355 (2006).

49. D. W. Felsher, J. M. Bishop, Transient excess of MYC activity can elicit genomic instability and tumorigenesis. *Proceedings of the National Academy of Sciences* **96**, 3940–3944 (1999).

50. J. Chappell, S. Dalton, Roles for MYC in the Establishment and Maintenance of Pluripotency. *Cold Spring Harbor Perspectives in Medicine* **3**, a014381–a014381 (2013).

51. X. Wang, Y. Ma, R. Xu, J. Ma, H. Zhang, S. Qi, J. Xu, X. Qin, H. Zhang, C. Liu, J. Chen, B. Li, H. Yang, Saijilafu, c□Myc controls the fate of neural progenitor cells during cerebral cortex development. *Journal of Cellular Physiology* **235**, 4011–4021 (2020).

52. M. Kang, J. J. A. Armenteros, G. S. Gulati, R. Gleyzer, S. Avagyan, E. L. Brown, W. Zhang, A. Usmani, N. Earland, Z. Wu, J. Zou, R. C. Fields, D. Y. Chen, A. A. Chaudhuri, A. M. Newman, Mapping single-cell developmental potential in health and disease with interpretable deep learning. *bioRxiv*, 2024.03.19.585637-2024.03.19.585637 (2024).

53. T.-C. He, A. B. Sparks, C. Rago, H. Hermeking, L. Zawel, L. T. da Costa, P. J. Morin, B. Vogelstein, K. W. Kinzler, Identification of c-MYC as a Target of the APC Pathway. *Science* **281**, 1509–1512 (1998).

54. Y.-H. Hao, M. C. Lafita-Navarro, L. Zacharias, N. Borenstein-Auerbach, M. Kim, S. Barnes, J. Kim, J. Shay, R. J. DeBerardinis, M. Conacci-Sorrell, Induction of LEF1 by MYC activates the WNT pathway and maintains cell proliferation. *Cell Communication and Signaling* **17**, 129–129 (2019).

55. L. Wang, C. Wang, J. A. Moriano, S. Chen, G. Zuo, A. Cebrián-Silla, S. Zhang, T. Mukhtar, S. Wang, M. Song, L. G. de Oliveira, Q. Bi, J. J. Augustin, X. Ge, M. F. Paredes, E. J. Huang, A. Alvarez-Buylla, X. Duan, J. Li, A. R. Kriegstein, Molecular and cellular dynamics of the developing human neocortex at single-cell resolution. *bioRxiv*, 2024.01.16.575956-2024.01.16.575956 (2024).

56. S. Repudi, I. Kustanovich, S. Abu-Swai, S. Stern, R. I. Aqeilan, Neonatal neuronal WWOX gene therapy rescues Wwox null phenotypes. *EMBO Molecular Medicine*, e14599 (2021).

57. M. Agostini, F. Romeo, S. Inoue, M. V. Niklison-Chirou, A. J. Elia, D. Dinsdale, N. Morone, R. A. Knight, T. W. Mak, G. Melino, Metabolic reprogramming during neuronal differentiation. *Cell Death & Differentiation* **23**, 1502–1514 (2016).

58. X. Zheng, L. Boyer, M. Jin, J. Mertens, Y. Kim, L. Ma, L. Ma, M. Hamm, F. H. Gage, T. Hunter, Metabolic reprogramming during neuronal differentiation from aerobic glycolysis to neuronal oxidative phosphorylation. *eLife* **5** (2016).

59. Y. Wei, Q. Miao, Q. Zhang, S. Mao, M. Li, X. Xu, X. Xia, K. Wei, Y. Fan, X. Zheng, Y. Fang, M. Mei, Q. Zhang, J. Ding, Y. Fan, M. Lu, G. Hu, Aerobic glycolysis is the

predominant means of glucose metabolism in neuronal somata, which protects against oxidative damage. *Nature Neuroscience* **26**, 2081–2089 (2023).

60. E. Di Lullo, A. R. Kriegstein, The use of brain organoids to investigate neural development and disease. *Nature Reviews Neuroscience 2017 18:10* **18**, 573–584 (2017).

61. A. A. Pollen, A. Bhaduri, M. G. Andrews, T. J. Nowakowski, O. S. Meyerson, M. A. Mostajo-Radji, E. Di Lullo, B. Alvarado, M. Bedolli, M. L. Dougherty, I. T. Fiddes, Z. N. Kronenberg, J. Shuga, A. A. Leyrat, J. A. West, M. Bershteyn, C. B. Lowe, B. J. Pavlovic, S. R. Salama, D. Haussler, E. E. Eichler, A. R. Kriegstein, Establishing Cerebral Organoids as Models of Human-Specific Brain Evolution. *Cell* **176**, 743-756.e17 (2019).

62. O. L. Eichmüller, J. A. Knoblich, Human cerebral organoids — a new tool for clinical neurology research. *Nature Reviews Neurology* **18**, 661–680 (2022).

63. F. Calegari, W. B. Huttner, An inhibition of cyclin-dependent kinases that lengthens, but does not arrest, neuroepithelial cell cycle induces premature neurogenesis. *Journal of Cell Science* **116**, 4947–4955 (2003).

64. C. Lange, W. B. Huttner, F. Calegari, Cdk4/CyclinD1 Overexpression in Neural Stem Cells Shortens G1, Delays Neurogenesis, and Promotes the Generation and Expansion of Basal Progenitors. *Cell Stem Cell* **5**, 320–331 (2009).

65. A. K. Bednarek, K. J. Laflin, R. L. Daniel, Q. Liao, K. A. Hawkins, C. M. Aldaz, WWOX, a Novel WW Domain-containing Protein Mapping to Human Chromosome 16q23.3–24.1, a Region Frequently Affected in Breast Cancer. *Cancer Research* **60**, 2140 LP – 2145 (2000).

66. N. Meyer, L. Z. Penn, Reflecting on 25 years with MYC. *Nature Reviews Cancer* **8**, 976–990 (2008).

67. R. Dhanasekaran, A. Deutzmann, W. D. Mahauad-Fernandez, A. S. Hansen, A. M. Gouw, D. W. Felsher, The MYC oncogene — the grand orchestrator of cancer growth and immune evasion. *Nature Reviews Clinical Oncology* **19**, 23–36 (2022).

68. E. S. Goetzman, E. V. Prochownik, The Role for Myc in Coordinating Glycolysis, Oxidative Phosphorylation, Glutaminolysis, and Fatty Acid Metabolism in Normal and Neoplastic Tissues. *Frontiers in Endocrinology* **9** (2018).

69. J. Liu, C. Zhang, W. Hu, Z. Feng, Tumor suppressor p53 and metabolism. *Journal of Molecular Cell Biology* **11**, 284–292 (2019).

70. L. Hertz, The Glutamate–Glutamine (GABA) Cycle: Importance of Late Postnatal Development and Potential Reciprocal Interactions between Biosynthesis and Degradation. *Frontiers in Endocrinology* **4** (2013).

71. C. M. Díaz-García, R. Mongeon, C. Lahmann, D. Koveal, H. Zucker, G. Yellen, Neuronal Stimulation Triggers Neuronal Glycolysis and Not Lactate Uptake. *Cell Metabolism* **26**, 361-374.e4 (2017).

72. K. F. Chau, M. L. Shannon, R. M. Fame, E. Fonseca, H. Mullan, M. B. Johnson, A. K. Sendamarai, M. W. Springel, B. Laurent, M. K. Lehtinen, Downregulation of ribosome biogenesis during early forebrain development. *eLife* **7** (2018).

73. R. M. Fame, M. L. Shannon, K. F. Chau, J. P. Head, M. K. Lehtinen, Concerted metabolic shift in early forebrain alters the CSF proteome and depends on cMYC downregulation for mitochondrial maturation. *Development*, doi: 10.1242/dev.182857 (2019).

74. S. J. Harrison-Uy, S. J. Pleasure, Wnt Signaling and Forebrain Development. *Cold Spring Harbor Perspectives in Biology* **4**, a008094–a008094 (2012).

75. Q. Gan, A. Lee, R. Suzuki, T. Yamagami, A. Stokes, B. C. Nguyen, D. Pleasure, J. Wang, H.-W. Chen, C. J. Zhou, Pax6 Mediates ß-Catenin Signaling for Self-Renewal and Neurogenesis by Neocortical Radial Glial Stem Cells. *Stem Cells* **32**, 45–58 (2014).

76. O. Machon, M. Backman, O. Machonova, Z. Kozmik, T. Vacik, L. Andersen, S. Krauss, A dynamic gradient of Wnt signaling controls initiation of neurogenesis in the mammalian cortex and cellular specification in the hippocampus. *Developmental Biology* **311**, 223–237 (2007).

77. W.-Y. Kim, X. Wang, Y. Wu, B. W. Doble, S. Patel, J. R. Woodgett, W. D. Snider, GSK-3 is a master regulator of neural progenitor homeostasis. *Nature Neuroscience* **12**, 1390–1397 (2009).

78. H.-Y. Wang, L.-I. Juo, Y.-T. Lin, M. Hsiao, J.-T. Lin, C.-H. Tsai, Y.-H. Tzeng, Y.-C. Chuang, N.-S. Chang, C.-N. Yang, P.-J. Lu, WW domain-containing oxidoreductase promotes neuronal differentiation via negative regulation of glycogen synthase kinase 3b. *Cell Death and Differentiation* **19**, 1049–1059 (2012).

79. S. Mohammadi, J. Davila-Velderrain, M. Kellis, A multiresolution framework to characterize single-cell state landscapes. *Nature Communications* **11**, 5399–5399 (2020).

80. I. Korsunsky, A. Nathan, N. Millard, S. Raychaudhuri, Presto scales Wilcoxon and auROC analyses to millions of observations. *bioRxiv*, 653253–653253 (2019).

81. Z. Gu, R. Eils, M. Schlesner, Complex heatmaps reveal patterns and correlations in multidimensional genomic data. *Bioinformatics* **32**, 2847–2849 (2016).

82. M. D. Robinson, D. J. McCarthy, G. K. Smyth, edgeR: a Bioconductor package for differential expression analysis of digital gene expression data. *Bioinformatics* **26**, 139–140 (2010).

83. L. Garcia-Alonso, C. H. Holland, M. M. Ibrahim, D. Turei, J. Saez-Rodriguez, Benchmark and integration of resources for the estimation of human transcription factor activities. *Genome Res.* **29**, 1363–1375 (2019).

84. G. Korotkevich, V. Sukhov, N. Budin, B. Shpak, M. N. Artyomov, A. Sergushichev, Fast gene set enrichment analysis. *bioRxiv*, 060012–060012 (2021).

85. F. Koopmans, P. van Nierop, M. Andres-Alonso, A. Byrnes, T. Cijsouw, M. P. Coba, L. N. Cornelisse, R. J. Farrell, H. L. Goldschmidt, D. P. Howrigan, N. K. Hussain, C. Imig, A. P. H. de Jong, H. Jung, M. Kohansalnodehi, B. Kramarz, N. Lipstein, R. C. Lovering, H. MacGillavry, V. Mariano, H. Mi, M. Ninov, D. Osumi-Sutherland, R. Pielot, K.-H. Smalla, H. Tang, K. Tashman, R. F. G. Toonen, C. Verpelli, R. Reig-Viader, K. Watanabe, J. van Weering, T. Achsel, G. Ashrafi, N. Asi, T. C. Brown, P. De Camilli, M. Feuermann, R. E. Foulger, P. Gaudet, A. Joglekar, A. Kanellopoulos, R. Malenka, R. A. Nicoll, C. Pulido, J.

de Juan-Sanz, M. Sheng, T. C. Südhof, H. U. Tilgner, C. Bagni, À. Bayés, T. Biederer, N. Brose, J. J. E. Chua, D. C. Dieterich, E. D. Gundelfinger, C. Hoogenraad, R. L. Huganir, R. Jahn, P. S. Kaeser, E. Kim, M. R. Kreutz, P. S. McPherson, B. M. Neale, V. O'Connor, D. Posthuma, T. A. Ryan, C. Sala, G. Feng, S. E. Hyman, P. D. Thomas, A. B. Smit, M. Verhage, SynGO: An Evidence-Based, Expert-Curated Knowledge Base for the Synapse. *Neuron* **103**, 217-234.e4 (2019).

Acknowledgments

We thank all members of the Aqeilan's and Davila-Velderrain's laboratories for technical help and fruitful discussion. Special thanks go to all WOREE and SCAR12 syndrome patients and families for their enduring support and dedication.

Funding:

WWOX foundation, Keren Shmuel Badihi (R.I.A.). R.I.A. holds the Jacob M. Eisenberg and Thomas W. Baylek Chair for Medical Research in the Field of Genetic Engineering. Fondazione Human Technopole (JDV)

Author contributions:
Conceptualization: DJS, AZ, JDV, RIA
Methodology: DJS, AZ, IR, IK, KM, SS
Investigation: DJS, AZ, JDV, RIA
Visualization: DJS, AZ, JDV
Supervision: JDV, RIA
Writing—original draft: DJS, AZ, JDV, RIA

Competing interests:
R.I.A. is a consultant for Mahzi Therapeutics. The other authors declare no competing interests.

Data and materials availability:
All data are available in the main text or the supplementary materials. The scRNA-seq data of all organoids are available at the functional genomics data collection (ArrayExpress) (ACCESION).

Figures and Tables

Fig. 1. Generation of patient-derived neural organoids

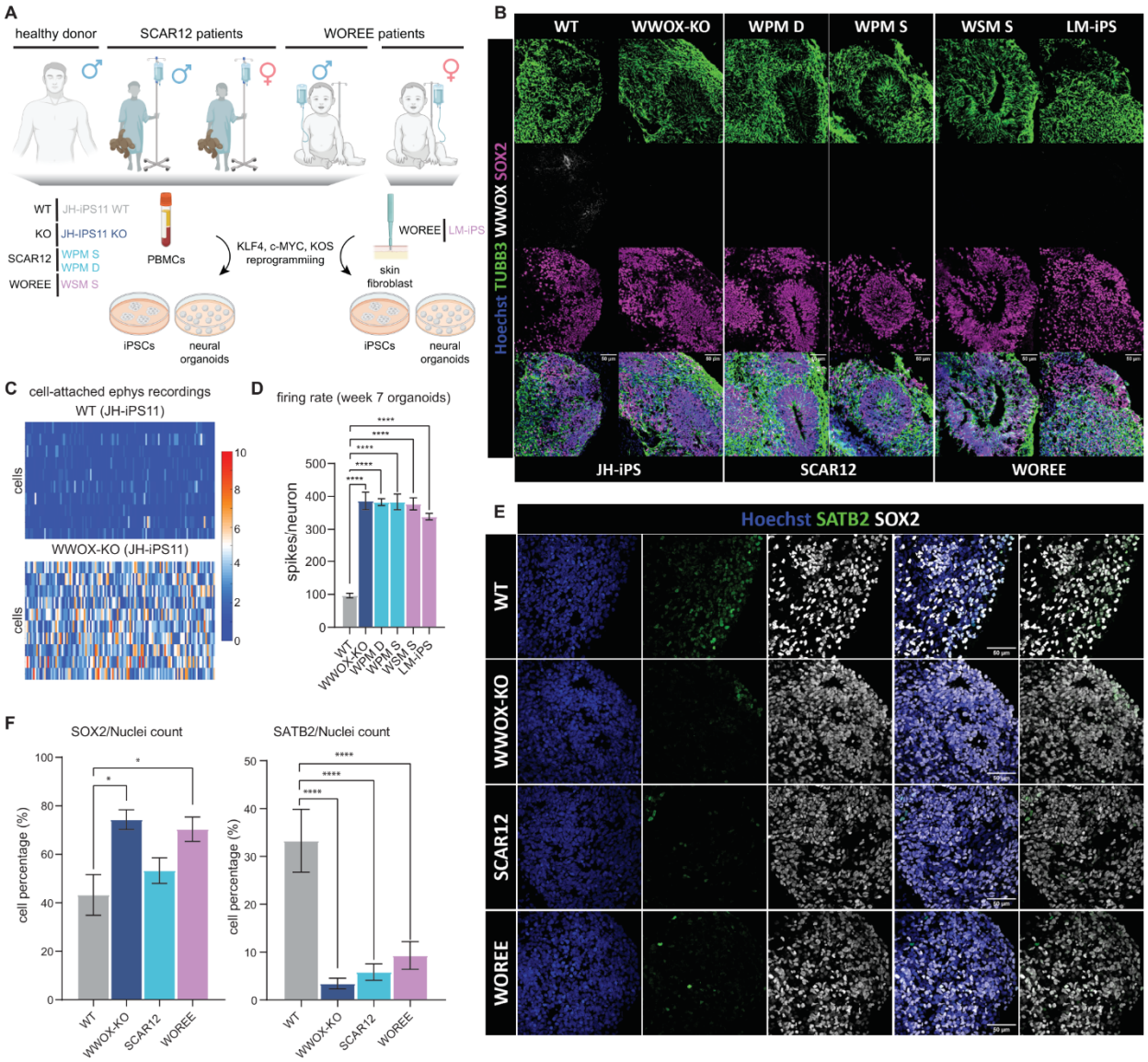

Fig. 1. Generation of patient-derived neural organoids. (A) Schematic representation of the research approach employed in this study. This Fig. highlights the different stem cell lines and experimental groups used. KOS; KLF4-OCT3/4-SOX2 Sendai vector, iPSCs; induced pluripotent stem cells. **(B)** Representative Immunofluorescent staining of the unguided organoids (previously termed cerebral organoids; COs) used in this study, showing the pan-radial glia (RG) marker SOX2, the new-born neurons and RG marker β3-tubulin (TUBB3) and WWOX at week 7 of culture. **(C)** Raster plots demonstrating selected neuronal firing from WT and WWOX-KO week 7 organoids over 4 minutes of cell-attached recording. **(D)** Quantification of all the cell-attached recordings obtained from WT, WWOX-KO, WOREE and SCAR12 organoids, including those exemplified in (B). (WT: n= 30 neurons; WWOX-KO: n=30; WPM S: n=21; WPM D: n=21; WSM S: n=24; LM-iPS: n=14). Statistical significance was determined by a one-way ANOVA test combined with Tukey's correction for multiple comparisons. **(E)** Immunostaining for SATB2, an early expressed neuronal marker and superficial-layer neurons at week 7 COs, together with SOX2. **(F)** Quantification of the data shown in (E) (WT: n= 3 neurons;

WWOX-KO: n=3; WPM S: n=3; WPM D: n=3; WSM S: n=3; LM-iPS: n=3). Statistical significance was determined using one-way ANOVA with Tukey's multiple comparisons test. n.s (non-significant), *$p \leq 0.05$, **$p \leq 0.01$, ***$p \leq 0.001$, ****$p \leq 0.0001$.

Fig. 2. scRNA-seq reveals population changes in WWOX-deficient organoids

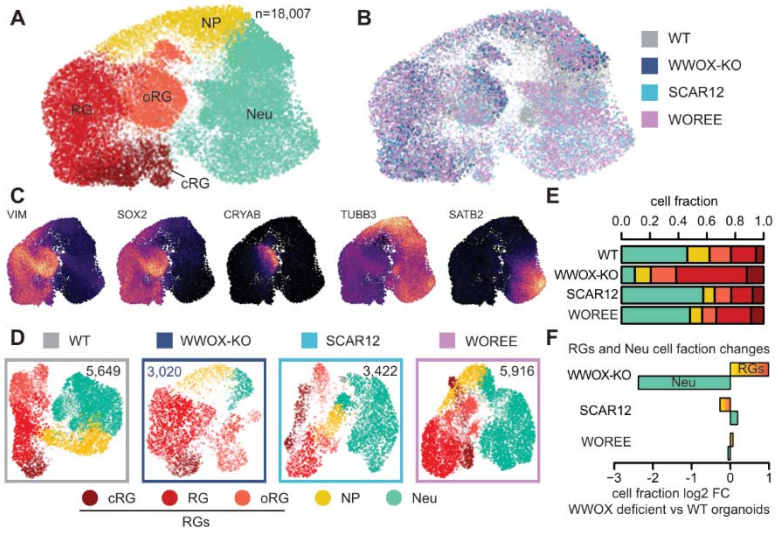

Fig. 2. scRNA-seq reveals population changes in WWOX-deficient organoids. (A) Two-dimensional uniform manifold approximation and projection (UMAP) representation of cells colored by annotated cell types from 4 cortical organoids (total number of cells = 18,007). **(B)** The UMAP presented in (A), colored by condition. **(C)** Feature plots of renown marker genes for radial glia (VIM, SOX2), outer-radial glia (CRYAB) and neurons (TUBB3, SATB2). **(D)** Individual UMAP representation for each tested condition, with total cell numbers reported. **(E)** Stacked bar representing the cell fraction for the identified cell types for each condition. **(F)** Cell populations fraction changes in WWOX-mutated organoids, calculated relative to the WT fraction and presented as log2 fold change. RG = radial glia, cRG = cycling radial glia, oRG = outer radial glia, NP = neural progenitor, Neu = neurons.

Fig. 3. MYC negatively correlates with WWOX in primary brain samples and is activated in radial glia cells upon WWOX-KO

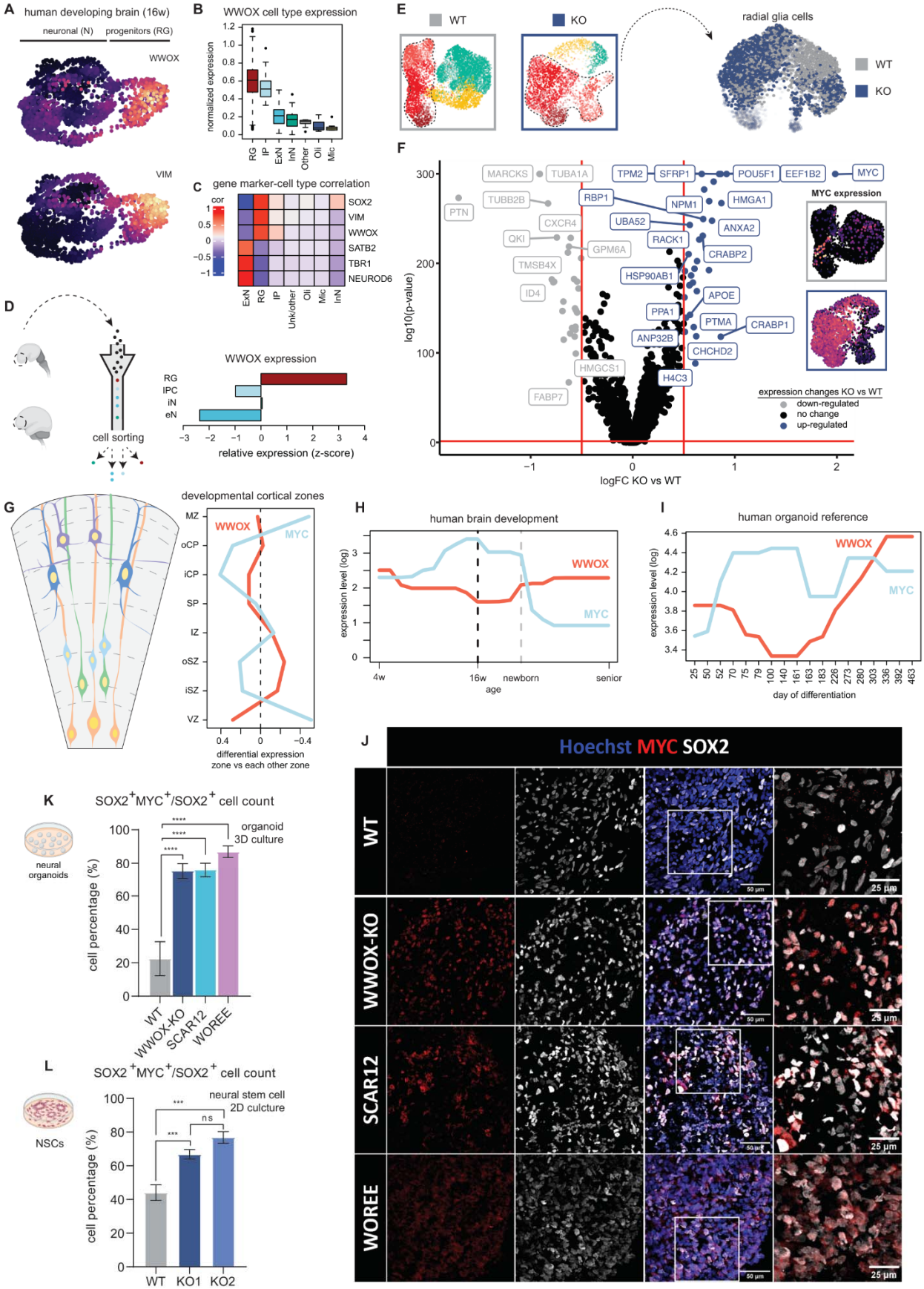

Fig. 3. MYC negatively correlates with WWOX in primary brain samples and is activated in radial glia cells upon WWOX-KO. **(A)** WWOX and VIM expression plot in post conceptional week 16 human fetal single-cell data (10.1016/j.cell.2021.07.039). **(B)** Normalized WWOX expression across cell types of the single-cell fetal data in panel A. **(C)** Correlation of normalized marker expression to cell type membership in human fetal single-cell data. **(D)** WWOX normalized expression in human fetal cell sorted data (10.1038/s41586-020-2825-4). **(E)** Radial glia isolation from WT and WWOX-KO organoid (n=4,548). **(F)** Differential gene expression in radial glia from WWOX-KO and WT organoids. Upregulated genes in the WWOX-KO are shown in blue, downregulated genes in the WWOX-KO in grey, not significant genes are in black. Red bars show threshold of significance, -log10 p-value > 1.30 (p-value = 0.05) and log2 fold change of ± 0.5. On the left, MYC expression in WT and WWOX-KO organoids. **(G)** (Left) Schematic of developing cortical zones, (Right) pairwise signature of WWOX and MYC expression in cortical zones from w21 (10.1038/nature13185). **(H)** Normalized expression of WWOX and MYC in brain development from embryonic stages (w04) to adulthood (senior) (10.1038/s41586-019-1338-5). Top MYC expression around the peak of neurogenesis (w16). **(I)** Cortical organoid reference from Gordon et al. 2021 (10.1038/s41593-021-00802-y) showing the opposite trend between WWOX and MYC in time (day of differentiation). **(J)** Immunostaining of week 16 organoids showing high colocalization of MYC and SOX2, suggesting higher localization of MYC to the nucleus of WWOX-mutated (WWOX-KO, WOREE and SCAR12) organoids. **(K)** Quantification of the representative images shown in (J) (WT: n=4 organoids; WWOX-KO: n=5; SCAR12: n=8; WOREE: n=7). Statistical significance was determined using one-way ANOVA with Tukey's multiple comparisons test. **(L)** 2D-cultured neural stem cells (NSCs) were immunostained for MYC, SOX2 and TUBB3 (see Supplementary Fig. 4C), and double-positive $SOX2^{+}MYC^{+}$ cells were quantified. The results are presented as fraction of the total $SOX2^{+}$ cells. Statistical significance was determined by a one-sided ANOVA test combined with Tukey's correction for multiple comparisons. n.s. (non-significant), * $p \leq 0.05$, ** $p \leq 0.01$, *** $p \leq 0.001$, **** $p \leq 0.0001$.

Fig. 4. WWOX-KO leads to G2/M and S arrest and cellular metabolism alterations

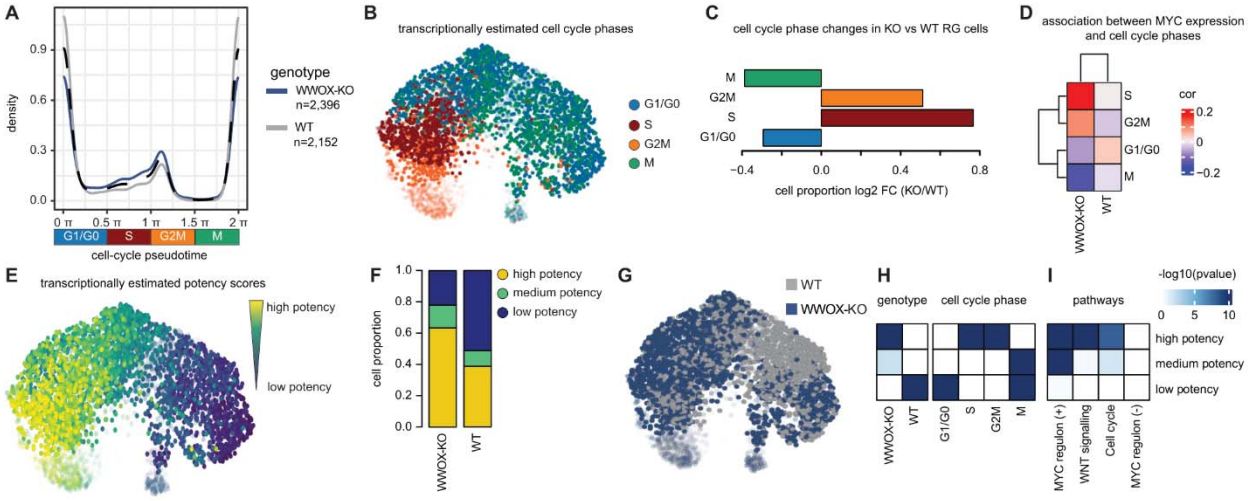

Fig. 4. WWOX-KO leads to G2/M and S arrest and cellular metabolism alterations. **(A)** Cell cycle phase inference in radial glia cells. Time points define a continuous scale of cell cycle states, that can be discretized as 0π - 0.5π as G1/G0 phase, 0.5π - 1π as S phase, 1π - 1.5π as G2M phase and 1.5π - 2π as M phase. The lines define how many radial glia cells are in a specific phase of the cell cycle (n=2,396 for WWOX-KO, n=2,152 for WT). **(B)** Cell landscape visualization of assigned cell cycle phase. **(C)** Log fold change of WWOX-KO on WT cell proportions across cell cycle phases, colored as in (B). **(D)** MYC normalized expression correlation to cell cycle phases showing high values for S and G2M phase in WWOX-KO organoids, and G1/G0 for WT. **(E)** UMAP colored by inferred potency scores. **(F)** Stacked bars quantifying potency states proportions in WWOX-KO and WT conditions. **(G)** Cell projection of organoid conditions. **(H)** Overrepresentation analysis of cells in each condition and cell cycle phase across potency states. High potency cells are overrepresented in WWOX-KO condition and in S - G2M phases, while Low potency in WT and G1/G0 - M phases. Medium potency cells are overrepresented in M phase, in WWOX-KO condition. **(I)** Enrichment analysis of metabolic gene sets in transcriptional signatures of potency states. High potency cells are enriched in WNT and cell cycle pathways, with targets regulated positively by MYC. Medium potency cells show similarly enrichment for MYC regulon and WNT. Low potency cells show no specificity. -log10(p-value) were capped to have a maximum score of 10.

Fig. 5. Neuronal population analysis in WT and patient-derived lines

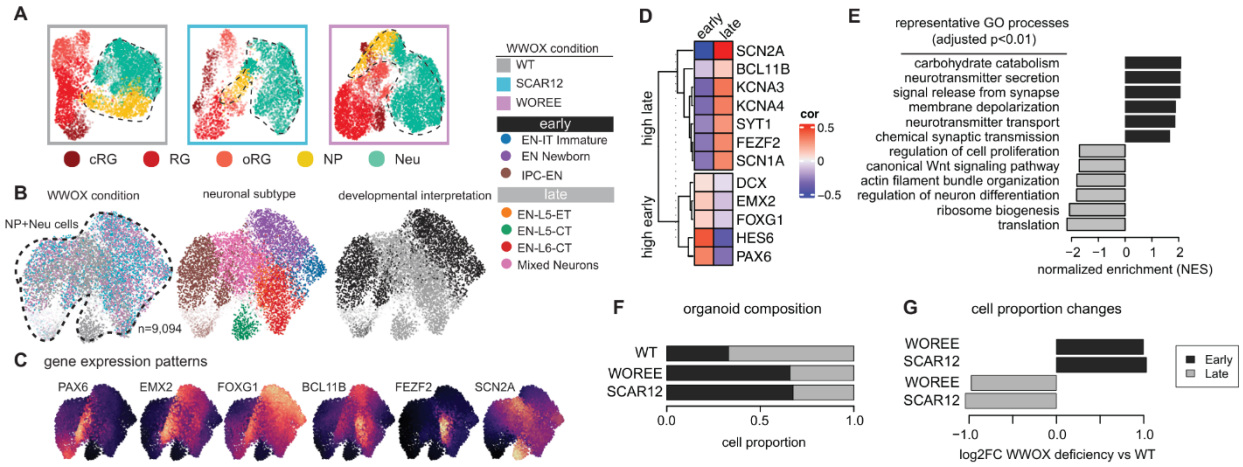

Fig. 5. Neuronal population analysis in WT and patient-derived lines. (A) Isolation of neural progenitors (in yellow) and neurons (in green) from WT, SCAR12 and WOREE conditions. **(B)** UMAP visualization of neural progenitors (NP) neuronal (Neu) cells colored by condition (left), assigned neuronal subtype (middle) and developmental categories (right). Identified categories are divided in early stages of neuronal development (dark grey) and late stages (light grey). **(C)** Feature plots of renown marker genes for progenitor cells (PAX6, EMX1, FOXG1) and neurons (BCL11B, FEZF2, SCN2A). **(D)** Marker gene normalized expression correlation to developmental categories ("Late" and "Early" neurons). **(E)** Representative Gene Ontology (GO) terms enriched in "late" cells compared to "early" cells, plotted as normalized enrichment score (NES). **(F)** Quantification of log fold change of early and late stages of neuronal subtypes across conditions. **(G)** Comparison of neuronal subtype proportions in patient lines compared to WT early and late stages.

Fig. 6. Neuronal restoration of WWOX using an AAV9 vector rescues functional abnormalities in WWOX-deficient organoids

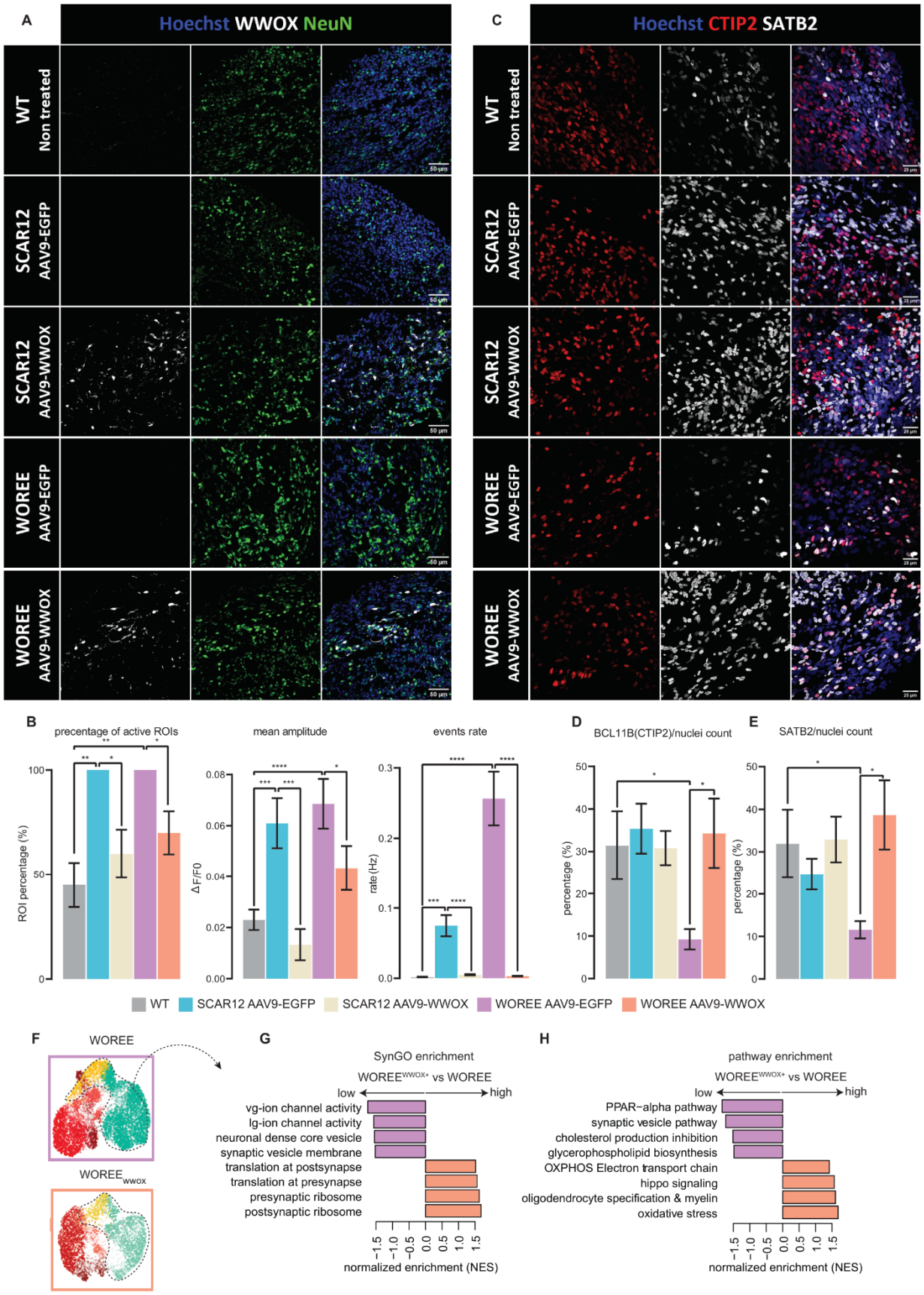

Fig. 6. Neuronal restoration of WWOX using an AAV9 vector rescued hyperexcitability and neuronal abnormalities in WWOX-deficient organoids. Week 10 COs were infected with either AAV9-SynI-EGFP-WPRE (AAV9-EGFP) or AAV9-SynI-WWOX-2A-EGFP-WPRE (AAV9-WWOX) and grown for 6 weeks. **(A)** Validation of the successful infection of week 16 COs with AAV9-WWOX (WT: n=4 organoids, SCAR12 AAV9-EGFP: n=8, SCAR12 AAV9-WWOX: n=8, WOREE AAV9-EGFP: n=7, WOREE AAV9-WWOX: n=7). **(B)** Neuronal activity visualized using Ca2+ recording in week 16 COs, comparing AAV9-EGFP and AAV9-WWOX infection. (WT: n=3 organoids, SCAR12 AAV9-EGFP: n=6, SCAR12 AAV9-WWOX: n=8, WOREE AAV9-EGFP: n=6, WOREE AAV9-WWOX: n=6). Statistical significance was determined using multiple t-tests, correcting for multiple comparisons by controlling the False Discovery Rate (FDR) using the Benjamini–Hochberg procedure. (Left) Percentage of active regions of interest (ROIs) within the imaged organoids. (Middle) Mean event amplitude, reflecting number of spiking neurons. (Right) Calcium events rate (WT: n=20 ROI, SCAR12 AAV9-EGFP: n=30, SCAR12 AAV9-WWOX: n=30, WOREE AAV9-EGFP: n=40, WOREE AAV9-WWOX: n=40). **(C)** The expression of cortical layers marks in week 16 organoids following the infection with either AAV9-EGFP or AAV9-WWOX, as shown by immunofluorescence stainings. **(D)** Quantification of CTIP2+ nuclei, divided by the total number of nuclei in each field counted. (WT: n=4 organoids, SCAR12 AAV9-EGFP: n=8, SCAR12 AAV9-WWOX: n=8, WOREE AAV9-EGFP: n=7, WOREE AAV9-WWOX: n=7). Statistical significance was determined by a one-way ANOVA test, correcting for multiple comparisons by controlling the FDR using the Benjamini–Hochberg procedure. **(E)** Quantification of SATB2+ nuclei, divided by the total number of nuclei in each field counted. (WT: n=4 organoids, SCAR12 AAV9-EGFP: n=8, SCAR12 AAV9-WWOX: n=8, WOREE AAV9-EGFP: n=7, WOREE AAV9-WWOX: n=7). Statistical significance was determined by a one-way ANOVA test, correcting for multiple comparisons by controlling the FDR using the Benjamini–Hochberg procedure. **(F)** Analysis of gene sets enrichment in neuronal progenitors and neurons in WOREE and WOREE-WWOX organoids. Bars represent normalized enrichment scores that are high in the treated organoid (salmon), related to synaptic compartment and translation, and low (lilac), associated to ion channel activity, both voltage-gated (vg) and ligand-gated(lg). **(G)** Pathway enrichment showing an increase OXPHOS and oxidative stress terms in WOREE-WWOX compared to WOREE, while downregulating pathways related to lipid metabolism. * $p \leq 0.05$, ** $p \leq 0.01$, *** $p \leq 0.001$, **** $p \leq 0.0001$.